

Topological transition from nodal to nodeless Zeeman splitting in altermagnets

Rafael M. Fernandes,^{1,*} Vanuildo S. de Carvalho,² Turan Birol,³ and Rodrigo G. Pereira⁴

¹*School of Physics and Astronomy, University of Minnesota, Minneapolis, Minnesota 55455, USA*

²*Instituto de Física, Universidade Federal de Goiás, 74.001-970, Goiânia-GO, Brazil*

³*Department of Chemical Engineering and Materials Science,*

University of Minnesota, Minneapolis, MN 55455, USA

⁴*International Institute of Physics and Departamento de Física Teórica e Experimental, Universidade Federal do Rio Grande do Norte, 59072-970 Natal-RN, Brazil*

(Dated: January 4, 2024)

In an altermagnet, the symmetry that relates configurations with flipped magnetic moments is a rotation. This makes it qualitatively different from a ferromagnet, where no such symmetry exists, or a collinear antiferromagnet, where this symmetry is a lattice translation. In this paper, we investigate the impact of the crystalline environment, enabled by the spin-orbit coupling, on the magnetic and electronic properties of an altermagnet. We find that, because each component of the magnetization acquires its own angular dependence, the Zeeman splitting of the bands has symmetry-protected nodal lines residing on mirror planes of the crystal. Upon crossing the Fermi surface, these nodal lines give rise to pinch points that behave as single or double type-II Weyl nodes. We show that an external magnetic field perpendicular to these mirror planes can only move the nodal lines, such that a critical field value is necessary to collapse the nodes and make the Weyl pinch points annihilate. This unveils the topological nature of the transition from a nodal to a nodeless Zeeman splitting of the bands. We also classify the altermagnetic states of common crystallographic point groups in the presence of spin-orbit coupling, revealing that a broad family of magnetic orthorhombic perovskites can realize altermagnetism.

I. INTRODUCTION

Altermagnetism refers to a broad range of magnetically ordered states that cannot be described in terms of standard ferromagnetic (F) or antiferromagnetic (AF) orders [1–14]. The distinguishing feature between these states is the type of crystalline symmetries that leave their spin configuration unchanged when combined with time reversal, i.e., with flipping the spins [2, 3]. In a ferromagnet, there is no such symmetry, hence the material acquires a non-zero magnetization. In a collinear antiferromagnet, translation by a lattice vector “undoes” time reversal, resulting in a non-zero staggered magnetization. In contrast, a lattice translation or inversion alone cannot undo the flipping of the spins of an altermagnetic (AM) state, but a rotation with respect to an axis or reflection with respect to a plane can. These distinct symmetry properties lead to important consequences, most notably on the Zeeman splitting of the band structure. To illustrate the differences between F, AF, and AM states, consider the following parametrization of the local magnetization $\mathbf{M}(\mathbf{r})$

$$\mathbf{M}(\mathbf{r}) = \mathbf{M}_0 d(\hat{\mathbf{r}}) \cos(\mathbf{Q} \cdot \mathbf{r}), \quad (1)$$

where $d(\hat{\mathbf{r}})$ is a function that depends only on the direction $\hat{\mathbf{r}}$ and \mathbf{Q} is the magnetic wave-vector. Upon time-reversal, $\mathbf{M}_0 \rightarrow -\mathbf{M}_0$ by definition. When $\mathbf{Q} = \mathbf{0}$ and $d(\hat{\mathbf{r}}) = 1$, it is not possible to undo the sign change of \mathbf{M}_0 , and one has a ferromagnet. In this case, the

spin degeneracy of the electronic states is lifted, resulting in a Zeeman splitting between the spin-up and spin-down bands. On the other hand, in the case of a commensurate collinear antiferromagnet for which $d(\hat{\mathbf{r}}) = 1$ and $2\mathbf{Q}$ is a reciprocal lattice vector, the sign change of \mathbf{M}_0 imposed by time reversal can be compensated by a translation by the appropriate lattice vector \mathbf{R} , since $\cos(\mathbf{Q} \cdot \mathbf{R}) = -1$. Therefore, the spin degeneracy is preserved, and the bands are not subjected to Zeeman splitting in the AF state.

There are other magnetic configurations given by Eq. (1), however, that cannot be described as either a F or an AF state. Consider, for example, the case where the wave-vector is trivial, $\mathbf{Q} = \mathbf{0}$, but the form factor $d(\hat{\mathbf{r}})$ is not, i.e. there is a crystalline symmetry operation \mathcal{R} such that $d(\mathcal{R}\hat{\mathbf{r}}) = -d(\hat{\mathbf{r}})$. For a centrosymmetric crystal, as long as this operation is not inversion (e.g. a rotation or a reflection), the spin degeneracy is lifted, causing a Zeeman splitting in the band structure that is neither uniform nor requires the presence of spin-orbit coupling (SOC). The resulting state is an example of an altermagnet [2–4, 11], a classification that also encompasses a range of magnetic systems that display non-relativistic Zeeman spin-splitting [15–19]. This distinction between F, AF, and AM states can be cast in formal grounds in terms of the three distinct types of spin groups – generalizations of magnetic groups in which rotations in spin space are decoupled from real space operations [2].

To shed further light on the nature of altermagnetism, and on its connection with other concepts of many-body electronic systems [3], it is useful to consider the special case of an isotropic system, for which $d(\hat{\mathbf{r}})$ can be expressed in terms of spherical harmonics $Y_{lm}(\hat{\mathbf{r}})$. In

* rfernand@umn.edu

the situation where l is positive and even, the AM order parameter in Eq. (1) can be understood as a magnetization with a non-zero angular momentum, corresponding to e.g. a d -wave or a g -wave “ferromagnet” [16]. These types of order parameter, in turn, naturally emerge within the well-understood Pomeranchuk instabilities of a Fermi liquid in the spin-triplet $l = 2$ or $l = 4$ channels, respectively [20]. Therefore, any even-parity, spin-triplet $l > 0$ Pomeranchuk instability of a metal, whose general properties were investigated in Ref. [21], results in an altermagnet; note, however, that an AM state can also be realized in insulators. An appealing realization of such a spin-triplet Pomeranchuk instability is the so-called nematic-spin-nematic state [21, 22], which corresponds to a d -wave modulation of the spin polarization, and displays unique collective modes.

The parametrization of $d(\hat{\mathbf{r}})$ in terms of spherical harmonics also allows us to conclude, via a straightforward calculation (see Appendix A), that the AM magnetic configuration described by Eq. (1) displays a higher-order magnetic multipole moment of $l + 1$ rank – i.e., a magnetic octupole for $l = 2$ or a magnetic dotriacontapole for $l = 4$, as opposed to the magnetic dipole condensed in ferromagnets ($l = 0$) [19, 23]. Multipolar orders [24–27] have been a common theme in studies of correlated f -electron systems [28, 29] and d -electron systems [30, 31] with strongly-coupled spin and orbital degrees of freedom. In the case of AM, the multipole moments can be understood as arising from the multipole expansion of the electronic spin density rather than from the electronic configuration of an isolated atom.

Finally, within a more microscopic description, the coarse-grained function $d(\hat{\mathbf{r}})$ can be attributed to intra-unit-cell “antiferromagnetism”, i.e. a non-trivial configuration of the magnetic moments of the atoms in a unit cell that yields a zero net magnetization and that does not break translational symmetry [15, 18]. It is important that the symmetry connecting opposite magnetic moments within the unit cell is not inversion, in which case one obtains instead of an altermagnet a compensated antiferromagnet with spin-degenerate bands (see, for example, the case of CuMnAs in Ref. [32]). The latter, in turn, is described by the same type of spin groups as an AF with non-zero wave-vector [2].

Thus, altermagnets have a close relationship with non- s -wave “ferromagnets,” multipolar magnets, or intra-unit-cell “antiferromagnets.” Previous works, which provided crucial insight about the properties of altermagnets, have primarily focused on the case in which the vector \mathbf{M}_0 in Eq. (1) can point in any direction [2–4, 33, 34]. Meanwhile, because of the ubiquitous presence of the SOC, the crystalline environment inevitably restricts the possible directions of the magnetic moments, even when the SOC is weak. Here, we investigate the impact of the coupling to the crystalline environment, and thus of the SOC, on the properties of an altermagnet. Our main finding is that the local magnetization in an altermagnet is generally not collinear, and that Eq. (1)

must be replaced by

$$\mathbf{M}(\mathbf{r}) = M_0 \mathbf{d}(\hat{\mathbf{r}}) \cos(\mathbf{Q} \cdot \mathbf{r}) . \quad (2)$$

The key point is that all three magnetization components acquire their own angular dependences rather than the same angular dependence as in Eq. (1). We use group theory to determine the properties of $\mathbf{d}(\hat{\mathbf{r}})$ for common crystallographic point groups, and illustrate it for the candidate AM compound MnF_2 . We also use these results to show that one of the magnetic phases proposed to be stabilized in orthorhombic perovskites with space group $Pnma$ is actually an AM phase that is not accompanied by a finite magnetization, thus opening a new avenue to search for altermagnets that do not display an anomalous Hall effect. We emphasize that Eq. (1) is a special case of Eq. (2), and that the two formulations do not contradict each other. In fact, as we show below, along high-symmetry crystallographic planes, only one of the components of $\mathbf{d}(\hat{\mathbf{r}})$ is non-zero, resulting in an effective collinear AM configuration (see also Ref. [11]).

To assess the impact of these results on the band structure of altermagnets, we solve the appropriate low-energy Hamiltonian and show that nodal lines emerge, along which the Zeeman splitting between the bands vanish. Remarkably, although topologically trivial with respect to non-spatial symmetries, these nodal lines lie on mirror planes of the crystal, and are thus protected by crystalline symmetries [35]. In altermagnetic metals, the Fermi surface acquires a non-trivial spin texture and is split in two everywhere except at the pinch points originating from the intersection with the nodal lines. Upon expanding the Hamiltonian around these pinch points and calculating their Berry phase, we find that the pinch points actually behave as type-II single or double Weyl nodes [36, 37].

The symmetry-protection of the nodal lines has crucial implications for the nature of the transition from an AM phase to a F phase driven by a uniform magnetic field. At first sight, one might have expected that the magnetic field would immediately generate a Zeeman splitting everywhere in the band structure, thus destroying the Fermi-surface pinch points that characterize AM metals. However, the nodal lines cannot be destroyed by an infinitesimal field that is perpendicular to the mirror plane along which the nodal lines lie. Instead, a small magnetic field leads to closed nodal loops that move along the mirror plane. Consequently, a fully Zeeman-split band structure, which is characteristic of a ferromagnetic phase, only emerges for a large enough magnetic field, which is necessary to collapse the nodal loops. Conversely, the Weyl-like pinch points of the Fermi surface located on the plane perpendicular to the field move towards each other and annihilate for a critical value of the field. Thus, the AM-F transition in which the Zeeman splitting of the bands changes from nodal to nodeless is a topological transition.

This paper is organized as follows: in Sec. II, we present a group-theoretical classification of AM states in

| Point group | AM irrep | $\mathbf{d}_i(\mathbf{k}) \equiv (d_{i,x}, d_{i,y}, d_{i,z})$ |
|-------------|------------|---|
| D_{2h} | A_{1g}^- | $(k_y k_z, \eta_1 k_x k_z, \eta_2 k_x k_y)$ |
| D_{4h} | A_{1g}^- | $(k_y k_z, -k_x k_z, \eta k_x k_y (k_x^2 - k_y^2))$ |
| | B_{1g}^- | $(k_y k_z, k_x k_z, \eta k_x k_y)$ |
| | B_{2g}^- | $(-k_x k_z, k_y k_z, \eta (k_x^2 - k_y^2))$ |
| D_{6h} | A_{1g}^- | $(k_y k_z, -k_x k_z, \eta k_x k_y (k_x^2 - 3k_y^2) (3k_x^2 - k_y^2))$ |
| | B_{1g}^- | $(k_x^2 - k_y^2, -2k_x k_y, \eta k_x k_z (k_x^2 - 3k_y^2))$ |
| | B_{2g}^- | $(2k_x k_y, k_x^2 - k_y^2, \eta k_y k_z (3k_x^2 - k_y^2))$ |
| | E_{2g}^- | $\begin{cases} (k_y k_z, k_x k_z, 2\eta k_x k_y) & , i = 1 \\ (k_x k_z, -k_y k_z, \eta (k_x^2 - k_y^2)) & , i = 2 \end{cases}$ |
| O_h | A_{1g}^- | $(k_y k_z (k_y^2 - k_x^2), k_x k_z (k_x^2 - k_y^2), k_x k_y (k_x^2 - k_y^2))$ |
| | A_{2g}^- | $(k_y k_z, k_x k_z, k_x k_y)$ |
| | E_g^- | $\begin{cases} \sqrt{3} (k_y k_z, -k_x k_z, 0) & , i = 1 \\ (-k_y k_z, -k_x k_z, 2k_x k_y) & , i = 2 \end{cases}$ |
| | T_{2g}^- | $\begin{cases} (k_x k_z, -k_y k_z, \eta (k_x^2 - k_y^2)) & , i = 1 \\ (\eta (k_y^2 - k_x^2), k_x k_y, -k_x k_z) & , i = 2 \\ (-k_x k_y, \eta (k_x^2 - k_y^2), k_y k_z) & , i = 3 \end{cases}$ |

TABLE I. Classification of the “pure” altermagnetic (AM) order parameters in the four point groups D_{2h} (orthorhombic), D_{4h} (tetragonal), D_{6h} (hexagonal), and O_h (cubic). The minus sign at the superscript of the irreducible representations (irreps) indicates that the order parameter is odd under time reversal. The third column shows the small-momentum expansion of the vector $\mathbf{d}_i(\mathbf{k})$ associated with each of the allowed AM order parameters. The parameters η_i are related to magnetic anisotropy and cannot be determined based on symmetry alone.

the presence of SOC. Sec. III introduces the effective low-energy models for AM and demonstrates their intrinsic non-collinearity. In Sec. IV, we show the emergence of symmetry-protected nodal lines in the Zeeman splitting of AM. The topological character of the transition from an altermagnetic to a ferromagnetic state is discussed in V. Sec. VI is devoted to the conclusions, whereas details of the model and of the calculations discussed in the main text are presented in Appendices A-F.

II. ALTERMAGNETS IN THE PRESENCE OF SOC

We start by employing group theory to classify the AM order parameter Φ^i (where i denotes different components) whose underlying crystalline environment, via the SOC, forces the magnetic moments to point along certain directions. For the magnetization \mathbf{m} , this implies that it must transform as the irreducible representations (irreps) of the crystallographic point group, rather than a vector in the space of rotations. For instance, in the tetragonal group D_{4h} , m_z transforms as the one-dimensional (1D) irrep A_{2g}^- , whereas (m_x, m_y) transform as the two-dimensional (2D) irrep E_g^- . Here, the minus superscript indicates that the quantity is odd under time reversal. The situation is analogous in the case of Φ^i . In the widely studied cases of AM states that preserve inversion and have zero wave-vector, Φ^i must transform as one of the time-reversal-odd, even-parity irreps of a centrosymmetric point group. We also add the constraint that the AM phase does not display a non-zero magneti-

zation, like a ferromagnet does. This excludes the irreps that transform as dipolar magnetic moments, such as the aforementioned A_{2g}^- and E_g^- in the tetragonal group D_{4h} . These “pure” AM phases should be distinguished from mixed AM-F phases, in which the onset of Φ^i necessarily triggers a non-zero magnetic moment. We will return to this point later.

The irreps of the AM order parameter for common point groups – orthorhombic D_{2h} , tetragonal D_{4h} , hexagonal D_{6h} , and cubic O_h – are shown in the first two columns of Table I. Extension to other point groups is straightforward. In most cases, Φ transforms as a 1D irrep, and thus behaves as an Ising-like order parameter [14]. The exceptions are the 2D irreps E_{2g}^- of the hexagonal group and E_g^- of the cubic group, where (Φ^1, Φ^2) behaves as a six-state clock-model order parameter, as well as the 3D irrep T_{2g}^- of the cubic group, in which (Φ^1, Φ^2, Φ^3) has the same free-energy as that of a Heisenberg ferromagnet with a cubic anisotropy term (see Appendix B). This analysis also makes the aforementioned connection between AM order and magnetic multipolar order explicit. Indeed, by using the crystallographic classification of multipoles of Ref. [23], one readily identifies the correspondence between Φ^i and different types of multipole moments of the electronic wave-function. For instance, Φ transforming as B_{1g}^- in the tetragonal group is equivalent to a magnetic octupole moment, as pointed out in Ref. [19], whereas (Φ^1, Φ^2, Φ^3) transforming as T_{2g}^- in the cubic group corresponds to magnetic quadrupolar toroidal moments.

Besides providing a sound framework to investigate the properties of altermagnets, which we pursue below, this

classification also offers interesting insights about candidate AM materials. Table I shows that, for orthorhombic crystals, there is only one allowed even-parity “pure” AM order parameter Φ , which transforms as A_{1g}^- . Interestingly, there is a broad class of orthorhombic materials known to display $\mathbf{Q} = 0$ magnetism: ABO_3 perovskites with space group $Pnma$, such as rare-earth titanates (LaTiO_3) and manganites (CaMnO_3) [38, 39]. In these systems, the ideal perovskite cubic crystal structure is distorted into an orthorhombic one by octahedral rotations that emerge to accommodate the A-site atom. Because of the expanded unit cell of the orthorhombic crystal structure shown in Fig. 1(a), magnetic orders characterized by a finite wave-vector in the ideal cubic structure become $\mathbf{Q} = 0$ magnetic orders in the $Pnma$ space group. The transformation properties of these intra-unit-cell “antiferromagnetic” states are well understood [38–40]. Comparing them with our classification of AM orders, we identify the so-called $G_a C_b A_c$ magnetic state [40] shown in Fig. 1(a) (or $A_a G_b C_c$ if $Pbnm$ axes are used for the orthorhombic cell) as an altermagnetic phase. In this notation, G_a means there is a G -type ordering (wave-vector (π, π, π) in the pseudocubic perovskite Brillouin zone) with magnetic moments pointing along the orthorhombic a -axis, superimposed with a C -type ordering (wave-vector $(\pi, \pi, 0)$) with magnetic moments along the b -axis (C_b) and an A -type ordering (wave-vector $(0, 0, \pi)$) with magnetic moments along the c -axis (A_c). While the known rare-earth titanates realize a different magnetic state with a non-zero ferromagnetic moment, dubbed $A_a F_b G_c$ in the notation above, DFT calculations show that the ground state energy of the AM $G_a C_b A_c$ phase is a close competitor [38]. Note that, as it follows from the analyses of Refs. [1, 41], the ground state $A_a F_b G_c$ with a dominant G_c component corresponds to an AM phase with a weak-ferromagnetic component [42, 43], which we here dubbed a mixed AM-F phase. The main difference with respect to the $G_a C_b A_c$ state is that only the former displays an anomalous Hall effect, which is observed experimentally in doped CaMnO_3 [44] and is related to the fact that the symmetries of that AM configuration allow for a non-zero macroscopic magnetization [45].

III. LOW-ENERGY MODELS FOR ALTERMAGNETS

While our group-theoretical results are not restricted to a particular model or material, in order to elucidate the coupling between Φ^i and the electronic degrees of freedom, it is useful to consider a general low-energy model. Thus, we start from a non-interacting single-band Hamiltonian $\mathcal{H}_0 = \sum_{\mathbf{k}} \varepsilon_{\mathbf{k}} c_{\mathbf{k}s}^\dagger c_{\mathbf{k}s}$, with electronic dispersion $\varepsilon_{\mathbf{k}}$ and electronic operator $c_{\mathbf{k}s}$, where \mathbf{k} is the momentum and s is the spin (summation over the spin indices is implicitly assumed in this paper). For simplicity, we assume that the orbital described by $c_{\mathbf{k}s}$ transforms as a one-dimensional irreducible representation (irrep) of

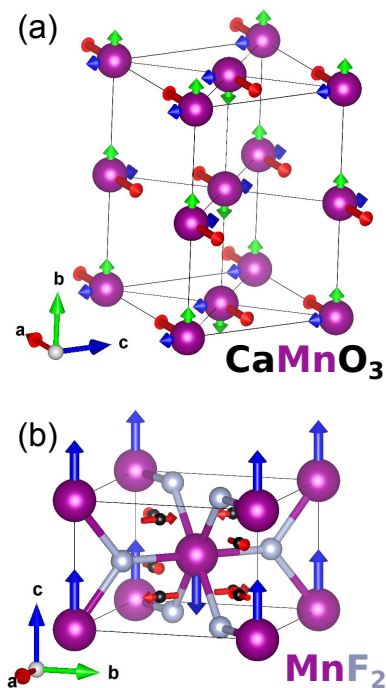


FIG. 1. **Non-collinearity of the magnetic moments in altermagnetic phases.** (a) The primitive unit cell of $Pnma$ CaMnO_3 contains four Mn ions (purple spheres). If G -type intra-unit-cell AF order along the a axis is present (the G_a order, shown as red arrows), the B-site moments are allowed to be tilted without reducing the symmetry. This leads to a C -type intra-unit-cell AF order along the b axis (the C_b order, green arrows), and an A -type order along the c axis (the A_c order, blue arrows). The resulting $G_a C_b A_c$ order is an altermagnetic state. The relative amplitude between the arrows were obtained from first principles calculations (see Appendices C-E). (b) The unit cell of MnF_2 contains 2 Mn ions (purple) and 4 F ions (grey). In the altermagnetic phase, the magnetic moments of the corner and the body-center Mn moments are antiparallel along the c axis. While all atomic moments are along c , the spin-density on the 8j Wyckoff site (shown as small black spheres) is non-collinear and displays the in-plane components shown in the figure.

the point group; generalizations to multi-orbital models are straightforward. The AM order parameter Φ^i must couple to a fermionic bilinear that transforms as the same irrep as Φ^i . To construct these bilinears, we extend the parametrization of the spatial-dependent magnetization in Eq. (1) to the momentum-dependent quantum spin-density, which is accomplished upon replacing \mathbf{M}_0 by the operator $c_{\mathbf{k}s}^\dagger \sigma_{ss'} c_{\mathbf{k}s'}$, where $\sigma_{ss'}^\mu$ are Pauli matrices (with $\mu = x, y, z$). Then, the interacting Hamiltonian \mathcal{H}_{int} that describes the coupling between the AM order parameter and the electrons is given by:

$$\mathcal{H}_{\text{int}} = -\lambda \sum_{\mathbf{k}, i} \Phi^i [\mathbf{d}_i(\mathbf{k}) \cdot \sigma_{ss'}] c_{\mathbf{k}s}^\dagger c_{\mathbf{k}s'}, \quad (3)$$

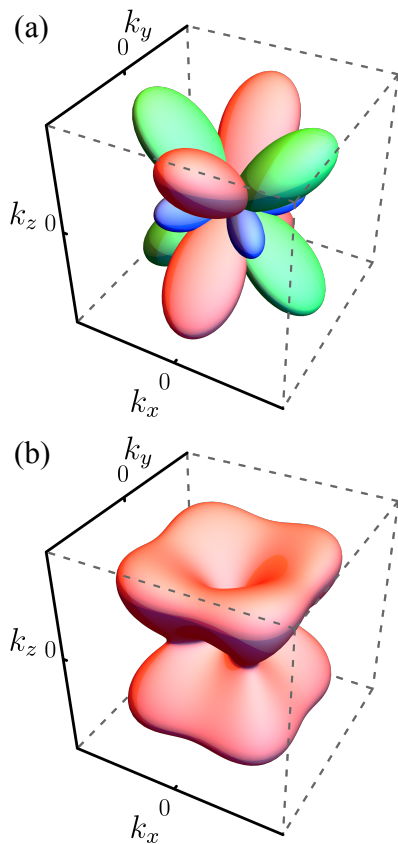


FIG. 2. **Polar plot of the d-vector $\mathbf{d}(\mathbf{k})$.** Panel (a) shows the squared three components d_μ^2 (red corresponds to d_x , green to d_y , and blue to d_z) while panel (b) shows the total magnitude $|\mathbf{d}|^2$. Here, we considered the specific case of an AM order parameter that transforms as the B_{1g}^- irrep of the tetragonal group D_{4h} , for which $\mathbf{d}(\mathbf{k}) = (k_y k_z, k_x k_z, \eta k_x k_y)$; we set $\eta = 3/4$ in this plot.

where λ is a coupling constant and the dot product refers to spin space, i.e. $\mathbf{d}_i(\mathbf{k}) \cdot \sigma_{ss'} = \sum_\mu d_{i,\mu}(\mathbf{k}) \sigma_{ss'}^\mu$. This is the analogue of Eq. (2) in momentum space. Recall that the index i refers to the number of components of the irrep that describes the AM order parameter. Since the transformation properties of Φ^i and of σ in terms of the irreps of each group are known, it is straightforward to determine the transformation properties of the set of vectors $\mathbf{d}_i(\mathbf{k})$. More specifically, the procedure is as follows: for a given point group \mathcal{G} , we know the time-reversal-odd irreps Γ_σ^- according to which the components of σ transform. Then, for a given AM order parameter Φ^i that transforms as one of the time-reversal-odd irreps Γ_Φ^- of \mathcal{G} that are different from Γ_σ^- , we determine the irreps Γ_d^+ of the components of \mathbf{d}_i such that $\mathbf{d}_i(\mathbf{k}) \cdot \sigma$ transforms as Φ^i , i.e. $\Gamma_d^+ \otimes \Gamma_\sigma^- = \Gamma_\Phi^-$. Once Γ_d^+ is determined, we construct the polynomials in Table I using group theory.

We note that the low-energy model in Eq. (3) has similarities with that employed in Ref. [21] to investigate the properties of spin-triplet Pomeranchuk instabilities. Indeed, as we discussed above, ordered states re-

sulting from even-parity spin-triplet Fermi liquid instabilities are altermagnets. While Ref. [21] considered the case of isotropic systems, here our focus is on the impact of the crystalline lattice. We also note that Eq. (3) is similar to that proposed in Ref. [46] to model spin-split bands in antiferromagnets without SOC, in which case functions analogous to $d_{i\mu}(\mathbf{k})$ described electric multipole moments arising from different types of intra-unit-cell “antiferromagnetism”. The main difference is that in Ref. [46] the spin coordinates transformed independently of the lattice.

Using the procedure described above, we obtain the irreps for each component of $\mathbf{d}_i(\mathbf{k})$ associated with a given AM order parameter Φ^i , as shown in the third column of Table I [47, 48]. Here, we consider only the lowest-order polynomials in momentum that give non-zero $d_{i,\mu}(\mathbf{k})$; these polynomials can also be expressed in terms of lattice harmonics by applying standard methods (see e.g. [49]). One important feature of $\mathbf{d}_i(\mathbf{k})$ is the presence of a prefactor η in some of its components. This parameter, which cannot be determined solely on symmetry grounds, is directly related to the magnetic anisotropy of the lattice. To illustrate this point, consider the case of the AM order parameter Φ that transforms as the B_{1g}^- irrep of the tetragonal group, which has been invoked to describe the rutile AM candidates MnF_2 and RuO_2 [2, 19]. Clearly, the combination $\sigma_z k_x k_y$ transforms as B_{1g}^- , since σ_z transforms as A_{2g}^- and $k_x k_y$, as B_{2g} . However, there is another combination of Pauli matrices and d-wave form-factors that also transforms as B_{1g}^- . Using the fact that (σ_x, σ_y) transforms as E_g^- while the doublet $(k_y k_z, -k_x k_z)$ transforms as E_g , we find that $(k_y k_z \sigma_x + k_x k_z \sigma_y)$ also transforms as B_{1g}^- . As a result, Φ must couple to both $\sigma_z k_x k_y$ and to $(k_y k_z \sigma_x + k_x k_z \sigma_y)$, but with different coupling constants. When expressed in terms of Eq. (3), we obtain $\mathbf{d}(\mathbf{k})$ as in Table I, with the parameter η corresponding precisely to the ratio between the two coupling constants. To illustrate the properties of $\mathbf{d}(\mathbf{k})$, we show in Fig. 2 a polar plot of the square of its three components d_μ^2 , as well as of its total magnitude $|\mathbf{d}|^2$, in the case of an AM order parameter that transforms B_{1g}^- in the tetragonal group D_{4h} . Note that, in the absence of SOC, only one of the components d_μ is non-zero.

We note that, in the presence of SOC, depending on the direction of the magnetic moments, altermagnetism may also trigger ferromagnetism. Consider, for instance, the AM state discussed above in the context of the rutiles, which is characterized by the d-wave form factor $k_x k_y$. Instead of an out-of-plane moment, let us instead assume that the moments point in the plane. The resulting two-component AM order parameter $\Phi \sim (k_x k_y \sigma_y, k_x k_y \sigma_x)$ transforms as the E_g^- irrep of D_{4h} . However, because the in-plane uniform magnetization $\mathbf{m} \sim (\sigma_x, \sigma_y)$ also transforms as E_g^- , the in-plane components of the $\mathbf{d}_i(\mathbf{k})$ vectors necessarily acquire trivial components proportional to the uniform magnetization, i.e. $\mathbf{d}_{1,\parallel}(\mathbf{k}) = (m_x, k_x k_y)$ and $\mathbf{d}_{2,\parallel}(\mathbf{k}) = (k_x k_y, m_y)$. We dub this type of order

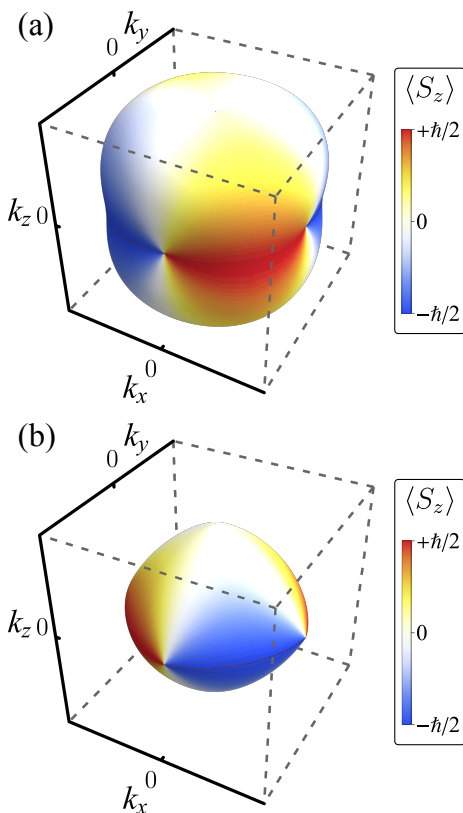


FIG. 3. **Spin texture of the Fermi surface of an altermagnetic metal.** Expectation value of the out-of-plane component of the spin S_z projected onto the two split Fermi surfaces of an altermagnetic metal, panels (a) and (b). Here, we consider the B_{1g}^- AM state of a tetragonal system. The non-interacting Fermi surface is assumed spherical for simplicity.

in which altermagnetism induces weak ferromagnetism a mixed AM-F phase. Although we will not discuss them further in the remainder of this paper, we note that AM configurations that allow an admixture with a weak ferromagnetic moment have been widely studied – indeed, this is the case of the RuO_2 compound in the presence of an in-plane field that is large enough to make the magnetic moments switch from out-of-plane to in-plane [1]. Of course, the distinction between pure and mixed AM phases is only meaningful in the presence of SOC, as they are described by the same spin group. Experimentally, a crucial difference between the pure AM and mixed AM-F phases is that only in the latter the system displays anomalous Hall effect or spontaneous Kerr rotation [2], as those effects are enabled by the same symmetries that allow for the admixture with a weak ferromagnetic moment. Indeed, as discussed elsewhere [50, 51], symmetry enforces the anomalous Hall effect to always be accompanied by a non-zero magnetization.

The results displayed in Table I show that the vector $d_{i,\mu}(\mathbf{k})$ never displays only a single component μ . Therefore, from Eq. (3), we conclude that the AM order

parameter corresponds to angular modulations of more than one spin polarization – or, in other words, that an AM phase is not collinear – when the magnetic and lattice degrees of freedom are coupled (see also Ref. [11]). This points to the fundamentally different role of SOC in AM and F systems, as in ferromagnets the magnetic anisotropy does not necessarily enforce non-collinearity.

In momentum space, the non-collinearity of the AM phase is manifested as a spin texture of the band structure. To illustrate this point, in Fig. 3 we show the expectation value of the out-of-plane spin component $S_z = \hbar\sigma_z/2$ projected onto the split Fermi surfaces inside the B_{1g}^- AM state of a tetragonal system. This result is obtained by diagonalizing the Hamiltonian containing Eq. (3) for a non-zero Φ ; for simplicity, we consider a non-interacting spherical Fermi surface. Clearly, the split Fermi surfaces display a rich spin texture. Nevertheless, we emphasize that along high-symmetry planes $\mathbf{d}(\mathbf{k})$ can point along a single direction. For instance, in the case of the B_{1g}^- AM phase shown in Fig. 3, $\mathbf{d}(\mathbf{k}) = k_x k_y \hat{\mathbf{z}}$ along the entire $k_z = 0$ plane, where $\langle S_z \rangle = \pm\hbar/2$; interestingly, this would correspond to the α -phase of the nematic-spin-nematic state introduced in Ref. [21]. Conversely, in the B_{1g}^- AM phase in a hexagonal system, $\mathbf{d}(\mathbf{k})$ at $k_z = 0$ points in-plane and has the same form as in the β -phase of Ref. [21]. We also note that, in a crystalline environment, magnetic multipolar moments of different ranks l are mixed. For example, in the case of B_{1g}^- or B_{2g}^- AM order parameters in the hexagonal group, while $(d_x\sigma^x + d_y\sigma^y)$ corresponds to a magnetic octupolar moment and $(d_x(\mathbf{k}), d_y(\mathbf{k}))$ is a d -wave form factor, $d_z\sigma^z$ corresponds to a magnetic hexadecapolar toroidal moment and $d_z(\mathbf{k})$ is a g -wave form factor (using the notation of Ref. [23]).

In real space, the non-collinearity of the AM state is associated with the fact that different magnetic Wyckoff sites allow different magnetic moment orientations and that there will always be a magnetic Wyckoff site with non-collinear moments in altermagnets. We illustrate it in Fig. 1(b) for the proposed AM phase of MnF_2 . Here, the magnetic symmetries of the Wyckoff sites occupied by the Mn and F atoms, labeled respectively 2a (purple) and 4f (grey), force the moments to point along the c axis, as shown in Fig. 1(b). Meanwhile, for the Wyckoff sites labeled 8j (black), the moments point in the plane, as expected for a magnetic octupole moment (see Appendices C-E for more details). Although these Wyckoff sites are not occupied by atoms in MnF_2 , the resulting non-collinearity of the spin-density will be manifested in the band structure in momentum space. Moreover, in other AM materials, the Wyckoff sites with non-collinear moments is not necessarily unoccupied. For instance, if the orthorhombic perovskite CaMnO_3 were to realize the intra-unit-cell “antiferromagnetic” phase $G_a C_b A_c$ discussed above, which corresponds to an A_{1g}^- AM order parameter, Fig. 1(a), obtained from DFT calculations, shows that every atom in the unit cell displays non-coplanar magnetic moments.

We end this section by noting an analogy between AM in the presence of SOC and unconventional superconductors. It has been pointed out the similarity between the d-wave Zeeman-splitting of an altermagnet with the gap function of a singlet d-wave superconductor [2]. On the other hand, Eq. (3) resembles the Hamiltonian of a *triplet* superconductor:

$$\mathcal{H}_{\text{SC}} = - \sum_{\mathbf{k}} \Delta [\mathbf{d}_{\text{SC}}(\mathbf{k}) \cdot \boldsymbol{\sigma}]_{ss'} c_{\mathbf{k}s}^\dagger (i\sigma_y c_{-\mathbf{k}}^\dagger)_{s'} + \text{h.c.} \quad (4)$$

The main difference is in the structures of the particle-hole and particle-particle condensates in spin space, which enforce the superconducting d-vector to be odd in momentum, $\mathbf{d}_{\text{SC}}(-\mathbf{k}) = -\mathbf{d}_{\text{SC}}(\mathbf{k})$, whereas the altermagnetic d-vector must be even, $\mathbf{d}(-\mathbf{k}) = +\mathbf{d}(\mathbf{k})$. Another consequence of this property is that the electronic spectrum of the superconductor consists of the sum in quadrature of the non-interacting and interacting coefficients:

$$E_{\pm}^{\text{SC}}(\mathbf{k}) = \pm \sqrt{\varepsilon_{\mathbf{k}}^2 + |\Delta|^2 |\mathbf{d}_{\text{SC}}(\mathbf{k})|^2}, \quad (5)$$

whereas the electronic spectrum of the altermagnets consists of the sum of the two terms, as we will show in Eq. (6).

IV. SYMMETRY-PROTECTED NODAL LINES OF THE ZEEMAN-SPLIT BANDS

We are now in position to investigate the properties of the electronic spectrum of an altermagnet in the presence of SOC. For simplicity, we first consider the case of an Ising-like AM order. Using Eq. (3), diagonalization of $\mathcal{H} = \mathcal{H}_0 + \mathcal{H}_{\text{int}}$ is straightforward and yields two dispersions:

$$E_{\pm}(\mathbf{k}) = \varepsilon_{\mathbf{k}} \pm \lambda \Phi |\mathbf{d}(\mathbf{k})|. \quad (6)$$

In agreement with previous works [3, 15, 17, 19, 24], we find a momentum-dependent Zeeman splitting of the bands, $\Delta E(\mathbf{k}) \equiv E_+(\mathbf{k}) - E_-(\mathbf{k})$, which in our case is given by $\Delta E(\mathbf{k}) \propto |\mathbf{d}(\mathbf{k})|$. Therefore, the Zeeman splitting only vanishes when the three components of $\mathbf{d}(\mathbf{k})$ are simultaneously zero. Because of the symmetry properties of $\mathbf{d}(\mathbf{k})$, this condition is not as restrictive as it may seem. Indeed, for all cases shown in Table I, the vector $\mathbf{d}(\mathbf{k})$ vanishes along either lines (for 1D irreps) or planes (for some multi-dimensional irreps) in momentum space, giving rise to nodal lines/planes in the band structure. In contrast, in the case where rotations in spin-space are decoupled from real space operations (i.e. in the absence of SOC), \mathbf{d} has effectively only one component. As a result, it vanishes along planes and the Zeeman splitting is characterized by nodal planes, as discussed in Ref. [5].

To shed further light on the nature of the Zeeman splitting nodes, we consider the specific case of an AM order

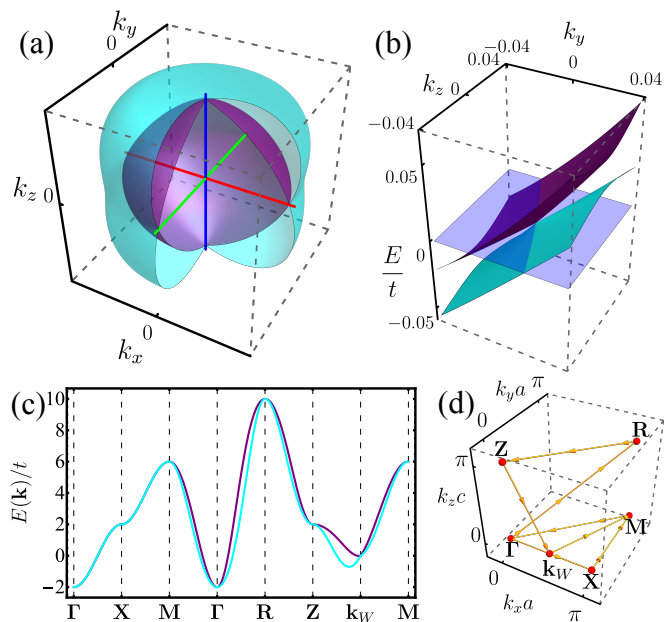


FIG. 4. **Nodal lines and Weyl-like Fermi-surface pinch points.** (a) Spin-splitting of the Fermi surface of an altermagnetic metal whose AM order parameter Φ transforms as the tetragonal B_{1g}^- irrep. Cyan and purple denote different Fermi surface sheets. Six pinch points where the Zeeman splitting vanishes emerge at the intersection with the nodal lines \mathcal{L}_x (red), \mathcal{L}_y (green), and \mathcal{L}_z (blue). For better visualization, the Fermi-surface sheets for $k_x > 0$ and $k_y < 0$ are not shown. (b) The electronic dispersion in the vicinity of the pinch point has the shape of a tilted cone, characteristic of a type-II Weyl node. (c) Zeeman splitting of a simple nearest-neighbor tight-binding dispersion $E(\mathbf{k})$ (in units of the electronic hopping t) in the AM state along the high-symmetry directions of the Brillouin zone shown in panel (d). The Weyl-like pinch point is located in this case at \mathbf{k}_W .

parameter Φ that transforms as B_{1g}^- in a tetragonal system. It follows from Table I that $\mathbf{d}(\mathbf{k}) = 0$ defines three nodal lines (\mathcal{L}_x , \mathcal{L}_y , \mathcal{L}_z) determined by the intersection between the three high-symmetry planes $k_x = 0$, $k_y = 0$, and $k_z = 0$, such that \mathcal{L}_x corresponds to $k_y = k_z = 0$, \mathcal{L}_y to $k_x = k_z = 0$ and \mathcal{L}_z to $k_x = k_y = 0$ (see also Ref. [5]). Along these lines, displayed respectively as red, green, and blue lines in Fig. 4(a), the Zeeman splitting of the band structure vanishes, as shown in Fig. 4(c) for the case of a simple nearest-neighbors tight-binding model (in this and the remainder figures, we set $\eta = 1/2$ for concreteness).

The topological properties of the nodal lines \mathcal{L}_α can be obtained from the symmetry properties of \mathcal{H}_{int} under time-reversal, charge-conjugation, and chiral operations. Following the tenfold classification of Ref. [35], we conclude that the nodal lines belong to class C of gapless topological phases, as they correspond to “Fermi surfaces” of codimension $p = 2$ that lie along high-symmetry directions. Thus, the nodal lines are topologically trivial with respect to non-crystalline symmetries. Nevertheless,

as shown in Ref. [35] (see also Ref. [52]), topologically trivial lines can still be protected by crystalline symmetries that leave \mathcal{H}_{int} invariant. This is precisely the case for the nodal lines \mathcal{L}_α : the two planes along which a given nodal line lies are actually vertical or horizontal mirror planes of the point group D_{4h} . Therefore, the AM nodal lines are symmetry-protected. Importantly, this conclusion holds for all AM orders in Table I that transform as a 1D irrep: as shown in Table IV in Appendix F, at least one of the planes along which a given nodal line lies is a crystallographic mirror plane. The case of multi-dimensional irreps is more subtle, as nodal planes also emerge for certain order-parameter configurations (see Appendix F).

The presence of symmetry-protected nodal lines in the AM state has important consequences for its low-energy electronic properties, particularly in the case of a metallic system. To show this, we once again focus on the case of a B_{1g}^- AM order parameter Φ in a tetragonal system with a generic parabolic dispersion $\varepsilon_{\mathbf{k}} = \frac{k^2}{2m} - \mu$. As shown in Fig. 4(a), the crossings between the three nodal lines $\{\mathcal{L}_x, \mathcal{L}_y, \mathcal{L}_z\}$ and the Fermi surface defines six pinch points where the Fermi surface is not Zeeman-split, $\mathbf{k}_{1\pm} = (\pm k_F, 0, 0)$, $\mathbf{k}_{2\pm} = (0, \pm k_F, 0)$ and $\mathbf{k}_{3\pm} = (0, 0, \pm k_F)$, with $k_F = \sqrt{2m\mu}$. Writing the Hamiltonian as $\mathcal{H} = \sum_{\mathbf{k}} c_{\mathbf{k}s}^\dagger H_{\mathbf{k}}^{ss'} c_{\mathbf{k}s'}$, expanding around k_{1+} , and defining $\mathbf{q} \equiv \mathbf{k} - \mathbf{k}_{1+}$, we obtain:

$$H_{\mathbf{q}} = v_F q_x \sigma^0 + \lambda \Phi k_F (q_z \sigma^y + \eta q_y \sigma^z), \quad (7)$$

with $v_F = k_F/m$. Using the results of Ref. [36], we identify $H_{\mathbf{q}}$ as the effective Hamiltonian of a type-II Weyl node. The dispersion around the pinch point, shown explicitly in Fig. 4(b), displays the characteristic tilted-cone structure of type-II Weyl points. The topological nature of the pinch points is further confirmed by a straightforward calculation of the Berry phase, which yields $\gamma = \pm\pi$ (see Appendix F). Beyond this specific case, we find that behaviors analogous to type-II Weyl nodes emerge at the intersections between the nodal lines and the Fermi surface for all 1D-irrep AM Φ order parameters of Table I. In the particular case of the B_{1g}^- and B_{2g}^- irreps of D_{6h} , these Weyl-like points have a Berry phase of $\gamma = \pm 2\pi$, and thus behave as double Weyl points [37] (see Appendix F). Note that these Weyl-like nodes are qualitatively different from actual Weyl points that can emerge in certain magnetically ordered states [53]. We emphasize that our main conclusions for the band structure of AM systems – i.e. the existence of symmetry-protected nodal lines – are enabled by the multi-component nature of the vector $\mathbf{d}(\mathbf{k})$, regardless of the magnitude of the anisotropy parameter η in Table I.

V. TOPOLOGICAL AM-F TRANSITION INDUCED BY AN EXTERNAL MAGNETIC FIELD

The existence of symmetry-protected nodal lines enabled by the SOC fundamentally impacts the response of an AM phase to a magnetic field. In the presence of a field \mathbf{h} , the Hamiltonian acquires a Zeeman term of the form $\mathcal{H}_Z = g_s \mu_B \sum_{\mathbf{k}} \mathbf{h} \cdot \boldsymbol{\sigma}_{ss'} c_{\mathbf{k}s}^\dagger c_{\mathbf{k}s'}$, where g_s denotes the effective g-factor and μ_B , the Bohr magneton. While in a paramagnet this term leads to a uniform Zeeman splitting of the electronic bands, $\Delta E_Z = g_s \mu_B h$, the situation in an altermagnet is qualitatively different. To see this, we note that \mathcal{H}_Z can be incorporated into \mathcal{H}_{int} in Eq. (3) provided that the vector $\mathbf{d}(\mathbf{k})$ is replaced by:

$$\tilde{\mathbf{d}}(\mathbf{k}) = \mathbf{d}(\mathbf{k}) - \frac{g_s \mu_B}{\lambda \Phi} \mathbf{h}. \quad (8)$$

The key point is that if the direction of the external field \mathbf{h} is perpendicular to one of the mirror planes protecting the AM nodal lines, the new \mathcal{H}_{int} will remain invariant under reflection with respect to the corresponding mirror. Consequently, the nodal lines that lie on that mirror plane will remain symmetry-protected even in the presence of \mathbf{h} . While this symmetry alone is not enough to ensure that a nodal line must exist, it does imply that if the nodal line exists before the application of the field, an infinitesimal field will not be able to gap it out, but only to move it along the mirror plane. Upon increasing the magnetic field, the nodal lines form closed loops that eventually collapse for a critical field value h_c , whose expression we give below. Thus, the momentum-dependent Zeeman splitting of the band structure, $\Delta E(\mathbf{k})$, is nodal for $h < h_c$ but nodeless for $h > h_c$. Since a nodal Zeeman splitting is a typical feature of an altermagnet, whereas a nodeless Zeeman splitting is characteristic of a ferromagnet, we denote the topological nodal-to-nodeless transition at h_c an AM-F transition.

It is instructive to illustrate these results in the specific case of a tetragonal B_{1g}^- AM order parameter. Consider first a field \mathbf{h} applied along $\hat{\mathbf{z}}$, which is perpendicular to the mirror plane where the zero-field nodal lines \mathcal{L}_x ($k_y = k_z = 0$) and \mathcal{L}_y ($k_x = k_z = 0$) are located. Solving $|\tilde{\mathbf{d}}(\mathbf{k})| = 0$, we find the condition $k_z = 0$, $k_x k_y = \frac{g_s \mu_B}{\lambda \Phi \eta} h$, which corresponds to two new nodal lines \mathcal{L}'_1 and \mathcal{L}'_2 . Note that the number of nodal lines decreases from 3 to 2 upon application of an infinitesimal magnetic field, because line \mathcal{L}_z is immediately gapped due to the fact that it does not lie on the relevant mirror plane. Like \mathcal{L}_x and \mathcal{L}_y , \mathcal{L}'_1 and \mathcal{L}'_2 are also located on the $k_z = 0$ plane; however, in contrast to the former, which are straight nodal lines, the latter are hyperbolic nodal lines. In the continuum, increasing h just moves the foci of the two hyperbolas to larger values of momentum. However, on the lattice, the new nodal lines form closed loops that collapse at a critical magnetic field value h_c . To determine h_c , we rewrite $\tilde{\mathbf{d}}(\mathbf{k})$ in terms of lattice harmonics and

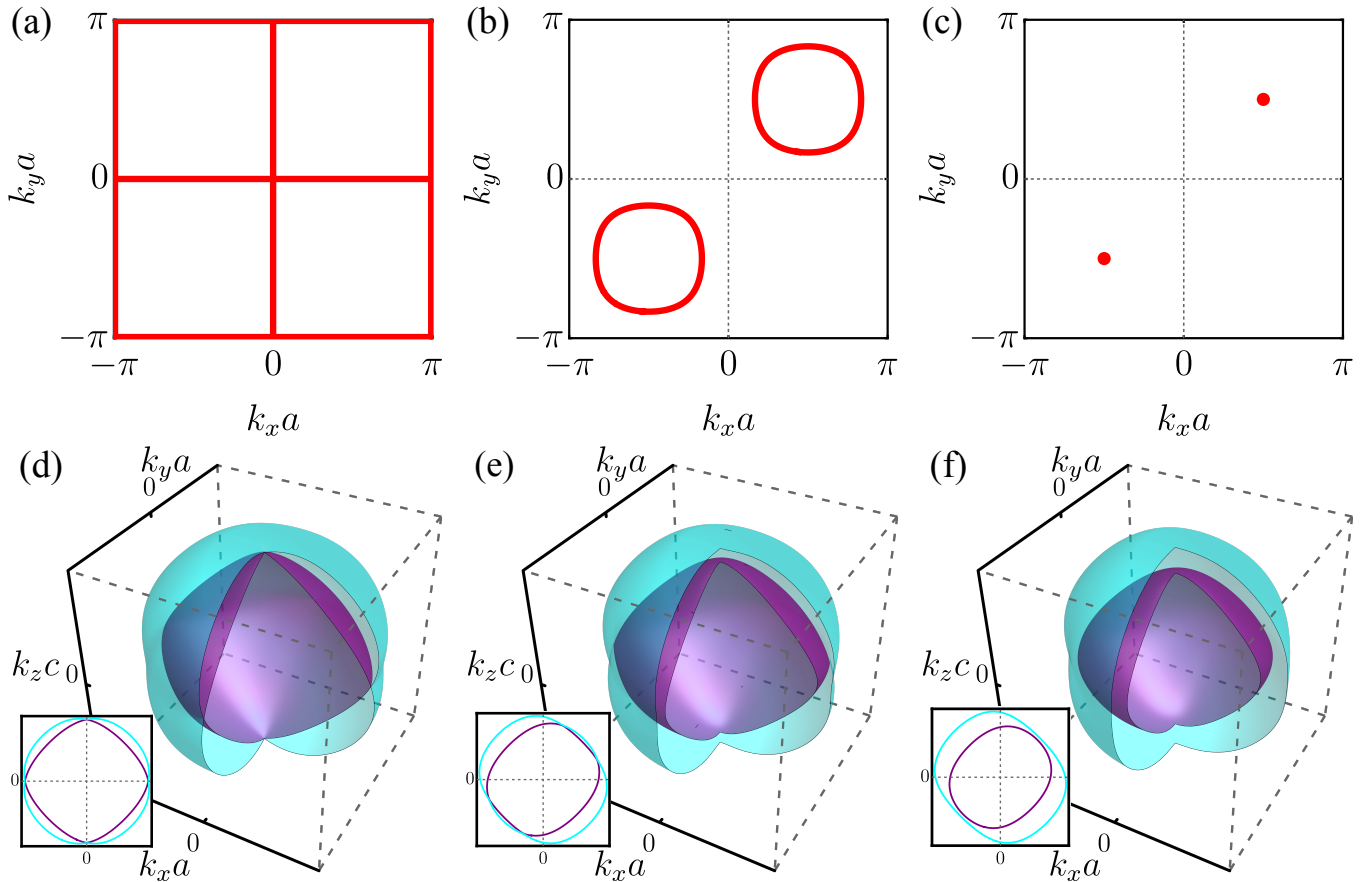


FIG. 5. **Impact of a magnetic field on the nodal lines and Weyl-like Fermi-surface pinch points.** In this figure, a magnetic field \mathbf{h} is applied along the z -axis of a tetragonal system with B_{1g}^- AM order. Panels (a)-(c) show the evolution of the nodal lines (red) on the $k_z = 0$ plane of the first Brillouin zone for $h = 0$, $h = h_c/2$, and $h = h_c \equiv \frac{\lambda\Phi\eta}{g_s\mu_B}$, respectively. As the field increases, the nodal lines form loops that collapse onto points at a critical value of the field. Panels (d)-(f) show the evolution of the split sheets of the Fermi surface for the same values of h ; the insets show the Fermi surfaces projected onto the $k_z = 0$ plane. Note that the pinch points, which behave as Weyl nodes, annihilate for a critical field $h_c^* < h_c$, such that for $h = h_c$ [panel (f)], the Fermi surfaces are disconnected. A simple nearest-neighbors tight-binding model was used to parametrize the band dispersion.

solve once again $|\tilde{\mathbf{d}}(\mathbf{k})| = 0$. The new nodal lines \mathcal{L}'_1 and \mathcal{L}'_2 are now described by the equations $\sin(k_z c) = 0$ and $\sin(k_x a) \sin(k_y a) = \frac{g_s\mu_B}{\lambda\Phi\eta} h$. As shown in Figs. 5(a)-(c), they describe nodal loops that collapse onto the points $\mathbf{k}_c = \pm \left(\frac{\text{sgn}(h)\pi}{2a}, \frac{\pi}{2a}, 0 \right)$ at a topological transition taking place at the critical value of the field

$$h_c \equiv \frac{\lambda\Phi\eta}{g_s\mu_B}. \quad (9)$$

Note that the location of the nodal loops on the $k_z = 0$ plane – first and third quadrants for $h > 0$ or second and fourth quadrants for $h < 0$ – breaks the tetragonal symmetry of the lattice down to orthorhombic by making the two in-plane diagonals inequivalent. This is a direct consequence of the fact that there is a trilinear term in the free energy coupling the B_{1g}^- AM order parameter Φ , the out-of-plane magnetic field h (which transforms as

A_{2g}^-), and the shear strain ε_{xy} (which transforms as B_{2g}^+ ; see also Refs. [14, 21, 54]).

Not surprisingly, the evolution of the Weyl-like pinch points as a function of an applied magnetic field mirrors that of the nodal lines. Figs. 5(d)-(f) show the Zeeman-split Fermi surface in the tetragonal B_{1g}^- AM ordered phase for different values of a field parallel to the $\hat{\mathbf{z}}$ axis; the insets show the Fermi surfaces projected onto $k_z = 0$. For $h < h_c^*$, the Fermi surface displays two pairs of Weyl nodes with opposite Berry phases located at $\mathbf{k}'_{1\pm} = \pm k_F(\kappa_+, \kappa_-, 0)$ and $\mathbf{k}'_{2\pm} = \pm k_F(\kappa_-, \kappa_+, 0)$, with $\kappa_{\pm} \equiv \text{sgn}(h)^{\frac{1\pm 1}{2}} \sqrt{1 \pm \sqrt{1 - \alpha^2}}/\sqrt{2}$ and $\alpha \equiv \frac{2g_s\mu_B h}{\lambda\Phi\eta k_F^2}$. At $h = h_c^*$, set by the condition $\alpha = 1$, the pairs of Weyl points \mathbf{k}'_{1+} and \mathbf{k}'_{2+} , as well as \mathbf{k}'_{1-} and \mathbf{k}'_{2-} , annihilate, resulting in fully split Fermi surfaces. Note that $h_c^* \leq h_c$, since the nodal lines will generally cease to cross the Fermi surface before they collapse. This behavior is analogous to the annihilation of nodes in su-

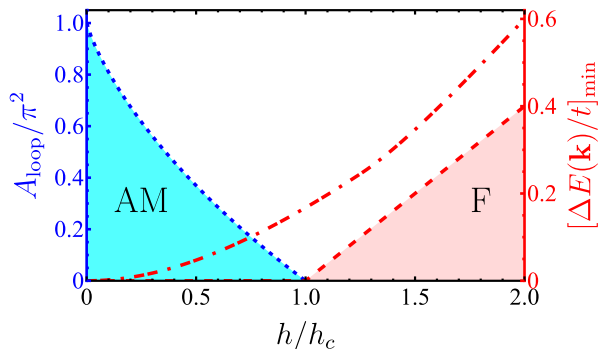


FIG. 6. **Field-driven altermagnetic (AM) to ferromagnetic (F) transition.** The “phase diagram” describes the transition between the tetragonal B_{1g}^- AM state, characterized by a nodal Zeeman splitting, and the F state, characterized by a nodeless Zeeman splitting. Here, A_{loop} (dashed blue line) refers to the area of the closed nodal lines on the $k_z = 0$ plane (see Fig. 5(b)), whereas $[\Delta E(\mathbf{k})]_{\text{min}}$ denotes the minimum value of the Zeeman splitting between the bands. When \mathbf{h} is along the z -axis, the AM-F transition is topological and occurs at the critical field $h_c = \frac{\lambda\Phi\eta}{g_s\mu_B}$ (dashed red line). For \mathbf{h} along the main diagonal of the $k_z = 0$ plane, the AM-F transition is trivial and takes place for an infinitesimal field (dash-dotted red line).

perconductors undergoing a nodal-to-nodeless transition [55–59]. The important difference is that, while in the superconducting case the gap function has a single angular dependence, in Eq. (6) the effective Zeeman-gap $|\mathbf{d}(\mathbf{k})|$ has three independent components that must simultaneously vanish to produce nodes.

In the case of a field applied along either the $\hat{\mathbf{x}}$ or $\hat{\mathbf{y}}$ axes, the analysis above remains almost unchanged, since these directions are also perpendicular to mirror planes on which two nodal lines reside, resulting in a topological nodal-to-nodeless transition. The main differences are: the value of the critical field, $h_c^{(x)} = h_c^{(y)} = h_c^{(z)}/\eta$, which reflects the magnetic anisotropy of the tetragonal lattice encoded by the parameter η ; and the lower monoclinic symmetry of the lattice, which reflects the triggering of an out-of-plane shear distortion $\varepsilon_{xz}/\varepsilon_{yz}$ by the magnetic field. This analysis illustrates that the critical field \mathbf{h}_c can be anisotropic and depends on parameters that vary among different materials.

The situation changes substantially, however, when the field is not applied along one of the three Cartesian axes. Consider, for example, a field applied along the in-plane diagonal $\mathbf{h} = \frac{1}{\sqrt{2}}(h, h, 0)$. The condition $|\tilde{\mathbf{d}}(\mathbf{k})| = 0$ now yields the system of equations $k_y k_z = \frac{g_s\mu_B}{\lambda\Phi\eta\sqrt{2}}h$, $k_x k_z = \frac{g_s\mu_B}{\lambda\Phi\eta\sqrt{2}}h$, and $k_x k_y = 0$, which does not admit a solution. Consequently, an infinitesimal field along this direction immediately gaps out all nodal lines, rendering the AM-F transition trivial. Fig. 6 illustrates the field-driven AM-F “phase diagram”, where the AM (F) phase is identified as that with nodal (nodeless) Zeeman splitting. The minimum Zeeman splitting, $[\Delta E(\mathbf{k})]_{\text{min}}$, is

only non-zero above the threshold z -axis field h_c , whereas the area of the nodal loops in Fig. 5(a)-(c) remains non-zero below h_c . For a field applied away from the high-symmetry directions, an infinitesimal field immediately triggers a $[\Delta E(\mathbf{k})]_{\text{min}} \neq 0$ (dot-dashed line). Importantly, while the results for the AM-F transition presented in Figs. 5 and 6 refer explicitly to the case of a B_{1g}^- AM order parameter in a tetragonal lattice, they apply to all ordered states of Table I whose order parameters transform as 1D irreps.

We note that in certain AM states, besides a magnetic field, strain can also be used to drive the topological AM-F transition even when there is no change in the magnetic ordering. This is because many AM states are piezomagnetic [10, 14], i.e. strain ε_{ij} induces a magnetic field component h_k according to $\varepsilon_{ij} = \Gamma_{ijk}h_k$, with the relevant piezomagnetic tensor elements Γ_{ijk} being proportional to the AM order parameter Φ . Therefore, in these cases, it is possible to use the appropriate strain components to generate a magnetic field and, consequently, induce the topological AM-F transition. In the specific case of a B_{1g}^- AM order parameter in the tetragonal lattice, in-plane shear strain ε_{xy} generates the out-of-plane magnetic field $h_z = \gamma\Phi\varepsilon_{xy}$, where γ is a coupling constant. The topological transition then takes place when $h_z = h_c^{(z)}$, which corresponds to a critical strain value $\varepsilon_{xy,c} = \frac{\lambda\eta}{\gamma g_s\mu_B}$ that is independent on Φ .

VI. CONCLUSIONS

In this paper we demonstrated the fundamental role that the crystalline environment plays on the magnetic and electronic properties of altermagnets. While in an isotropic altermagnet the magnitude of the magnetization develops an angular dependence, $\mathbf{M} = d(\hat{\mathbf{r}})(M_{0,x}, M_{0,y}, M_{0,z})$, in a crystalline environment each component of the magnetization acquires a different angular dependence, $\mathbf{M} = M_0(d_x(\hat{\mathbf{r}}), d_y(\hat{\mathbf{r}}), d_z(\hat{\mathbf{r}}))$. The resulting group theory classification of the AM order parameters also suggests new routes to search for altermagnetic states, such as the $Pnma$ perovskites that realize the $G_a C_b A_c$ magnetic state. The angular modulation of multiple components of the magnetization in altermagnets leaves clear fingerprints on their electronic structures, in the form of symmetry-protected nodal lines along crystallographic mirror planes and Fermi-surface pinch points that behave as type-II Weyl nodes. As a result, for magnetic fields applied along certain high-symmetry directions of the crystal, the transition from a nodal to a nodeless Zeeman splitting of the band structure, which we identify as an AM-F transition, not only requires a critical magnetic field but is also topological. Beyond the non-interacting band structure, these symmetry-protected nodal lines should also impact other electronic properties of altermagnets. This includes interaction-driven instabilities towards new electronic states, such as superconductivity, whose interplay

with altermagnets has been recently proposed to be a fertile ground for new phenomena [60–66].

ACKNOWLEDGMENTS

We thank J. Sinova and L. Šmejkal for fruitful discussions. RMF was supported by the Air Force Office of Scientific Research under Award No. FA9550-21-1-0423. TB was supported by the NSF CAREER grant DMR-2046020. RGP was supported by a grant from the Simons Foundation (Grant Number 1023171) and by the National Council for Scientific and Technological Development - CNPq.

APPENDIX A: RELATIONSHIP BETWEEN ALTERMAGNETISM AND MULTIPOLAR MAGNETISM

Here we show that the order parameter of an isotropic AM state is equivalent to a magnetic multipole moment. Following the main text, we parametrize the magnetization in the isotropic AM state as:

$$\mathbf{M}(\mathbf{r}) = \mathbf{M}_0 Y_{l_0 m_0}(\hat{\mathbf{r}}), \quad (\text{A1})$$

where \mathbf{M}_0 is a vector and $Y_{l_0 m_0}(\hat{\mathbf{r}})$ is one of the spherical harmonics. We want to compute the magnetic multipole moments μ_{lm} of this magnetization function. The definition is [27]:

$$\mu_{lm} \equiv \sqrt{\frac{4\pi}{2l+1}} \int \mathbf{M}(\mathbf{r}) \cdot \nabla (r^l Y_{lm}^*(\hat{\mathbf{r}})) d^3r. \quad (\text{A2})$$

We assume that the magnetization is contained within a sphere of radius R . For simplicity, we choose \mathbf{M}_0 to be parallel to the z -axis, i.e. $\mathbf{M}_0 = M_0 \hat{\mathbf{z}}$. Then:

$$\mu_{lm} \equiv M_0 \sqrt{\frac{4\pi}{2l+1}} \int Y_{l_0 m_0}(\hat{\mathbf{r}}) \partial_z (r^l Y_{lm}^*(\hat{\mathbf{r}})) r^2 d\Omega. \quad (\text{A3})$$

We have

$$\begin{aligned} \partial_z (r^l Y_{lm}^*) &= (\partial_z r^l) Y_{lm}^* + r^l (\partial_z Y_{lm}^*) \\ &= r^{l-1} [l \cos \theta Y_{lm}^* - \sin \theta \partial_\theta Y_{lm}^*], \end{aligned} \quad (\text{A4})$$

where we used $\partial_z = -\frac{\sin \theta}{r} \partial_\theta$. To proceed, it is convenient to write down the formal definition of Y_{lm} in terms of the associated Legendre polynomials P_{lm} :

$$Y_{lm}^* = (-1)^m \sqrt{\frac{(2l+1)(l-m)!}{4\pi(l+m)!}} P_{lm}(\cos \theta) e^{-im\varphi}. \quad (\text{A5})$$

To simplify the first term in Eq. (A4), we use the identity (hereafter we use a comma to separate the subscripts in order to avoid confusion):

$$x P_{l,m}(x) = \frac{(l-m+1)}{(2l+1)} P_{l+1,m}(x) + \frac{(l+m)}{(2l+1)} P_{l-1,m}(x). \quad (\text{A6})$$

From it, we obtain:

$$\begin{aligned} \cos \theta Y_{l,m}^* &= \sqrt{\frac{(l-m+1)(l+m+1)}{(2l+1)(2l+3)}} Y_{l+1,m}^* \\ &+ \sqrt{\frac{(l-m)(l+m)}{(2l+1)(2l-1)}} Y_{l-1,m}^*. \end{aligned} \quad (\text{A7})$$

To simplify the second term in Eq. (A4), we first rewrite it as

$$-\sin \theta \partial_\theta Y_{lm}^* = \sin^2 \theta \partial_{(\cos \theta)} Y_{lm}^* \stackrel{x \rightarrow \cos \theta}{=} (1-x^2) \partial_x Y_{lm}^*. \quad (\text{A8})$$

We now use the identity:

$$\begin{aligned} (1-x^2) \partial_x P_{l,m}(x) &= \frac{(l+1)(l+m)}{(2l+1)} P_{l-1,m}(x) \\ &- \frac{l(l-m+1)}{(2l+1)} P_{l+1,m}(x), \end{aligned} \quad (\text{A9})$$

and obtain

$$\begin{aligned} -\sin \theta \partial_\theta Y_{l,m}^* &= (l+1) \sqrt{\frac{(l-m)(l+m)}{(2l+1)(2l-1)}} Y_{l-1,m}^* \\ &- l \sqrt{\frac{(l-m+1)(l+m+1)}{(2l+1)(2l+3)}} Y_{l+1,m}^*. \end{aligned} \quad (\text{A10})$$

Substituting Eqs. (A7) and (A10) in (A4) gives

$$\partial_z (r^l Y_{l,m}^*) = r^{l-1} \sqrt{\frac{(2l+1)(l-m)(l+m)}{(2l-1)}} Y_{l-1,m}^*. \quad (\text{A11})$$

Substituting back in Eq. (A3) yields

$$\begin{aligned} \mu_{lm} &= M_0 \sqrt{\frac{4\pi(l-m)(l+m)}{(2l-1)}} \left[\int_0^R r^{l+1} dr \right] \\ &\times \left[\int Y_{l_0, m_0}(\hat{\mathbf{r}}) Y_{l-1,m}^*(\hat{\mathbf{r}}) d\Omega \right]. \end{aligned} \quad (\text{A12})$$

The final result is:

$$\mu_{lm} = \frac{3R^{l_0} \mathcal{M}}{l_0 + 3} \sqrt{\frac{(l_0 - m_0 + 1)(l_0 + 1 + m_0)}{4\pi(2l_0 + 1)}} \delta_{l, l_0 + 1} \delta_{m, m_0}, \quad (\text{A13})$$

where, in the last step, we used the fact that $V = \frac{4}{3}\pi R^3$ is the volume and defined the total magnetic moment $\mathcal{M} \equiv M_0 V$. For a system with uniform magnetization, $l_0 = 0$ and $m_0 = 0$, such that $M(\mathbf{r}) = \mathbf{M}_0 / \sqrt{4\pi}$, we obtain

$$(\mu_{lm})_{\text{dipole}} = \frac{\mathcal{M}}{\sqrt{4\pi}} \delta_{l,1} \delta_{m,0} = \left[\int M(\mathbf{r}) d^3r \right] \delta_{l,1} \delta_{m,0}, \quad (\text{A14})$$

which indeed corresponds to a magnetic dipole moment, since $l = 1$. Therefore, we conclude that the parametrization of the magnetization in Eq. (A1) corresponds to a multipole magnetic moment of rank $l = l_0 + 1$.

APPENDIX B: ALTERMAGNETIC LANDAU FREE-ENERGY EXPANSION

Here we derive the Landau free-energy expansions of the altermagnetic states described in Table I of the main text. There are three different types of AM order parameters depending on the irreps under which they transform: 1D irreps, in which case the AM order parameter has a single component Φ ; 2D irreps, in which case the AM order parameter has two components $\Phi = (\Phi^1, \Phi^2)$; and 3D irreps, in which case $\Phi = (\Phi^1, \Phi^2, \Phi^3)$.

The single-component AM order parameter Φ corresponds to most of the cases shown in Table I of the main text. In this situation, using standard methods [47, 48], the Landau free-energy is given by

$$F = \frac{a}{2} \Phi^2 + \frac{u}{4} \Phi^4, \quad (\text{B1})$$

and the AM order parameter is Ising-like. There are two cases in which the AM order parameter has two components: when it transforms as the E_{2g}^- irrep of D_{6h} or as the E_g^- irrep of O_h . In both cases, the Landau free-energy expansion has the same form. Parametrizing $\Phi = \Phi(\cos \alpha, \sin \alpha)$, we find

$$F = \frac{a}{2} \Phi^2 + \frac{u}{4} \Phi^4 + \frac{w}{6} \Phi^6 + \frac{\gamma}{6} \Phi^6 \cos 6\alpha. \quad (\text{B2})$$

This is the same Landau free-energy expansion of the six-state clock model. Minimization with respect to α gives $\alpha_0 = 2n\pi/6$ for $\gamma < 0$ or $\alpha_0 = (2n+1)\pi/6$ for $\gamma > 0$ with $n = 0, 1, \dots, 5$. Alternatively, we can express it as $\alpha_0 = p\pi/6$, with $p \in \mathbb{Z}$ even for $\gamma < 0$ and odd for $\gamma > 0$.

In Table I of the main text, there is only one case in which the AM order parameter has three components, which corresponds to the situation in which it transforms as the T_{2g}^- irrep of O_h . In this case, we have $\Phi = (\Phi^1, \Phi^2, \Phi^3)$ and the Landau free-energy expansion:

$$F = \frac{a}{2} \Phi^2 + \frac{u}{4} \Phi^4 + \frac{\gamma}{4} (\Phi_1^2 \Phi_2^2 + \Phi_1^2 \Phi_3^2 + \Phi_2^2 \Phi_3^2), \quad (\text{B3})$$

where $\Phi^2 \equiv \Phi_1^2 + \Phi_2^2 + \Phi_3^2$. The ground state Φ_0 is given by the sixfold-degenerate manifold $\pm(1, 0, 0)$, $\pm(0, 1, 0)$, and $\pm(0, 0, 1)$ for $\gamma > 0$, and by the eight-fold degenerate manifold $\pm(1, 1, 1)$, $\pm(1, -1, -1)$, $\pm(-1, 1, -1)$, and $\pm(-1, -1, 1)$, for $\gamma < 0$.

APPENDIX C: FIRST PRINCIPLES METHODS

First principles calculations were performed using the Vienna ab Initio Simulation Package (VASP) [67–69]. The values reported are calculated using the PBE exchange-correlation functional, and tested that the use of LDA gives comparable results.[70] A $16 \times 16 \times 24$ k-grid for MnF_2 , and a $8 \times 4 \times 8$ k-grid for CaMnO_3 were

| | | |
|----|----|--|
| Ca | 4c | $(x, 1/4, z 0, m_y, 0)$ |
| | | $(x + 1/2, 1/4, -z + 1/2 0, -m_y, 0)$ |
| | | $(-x, 3/4, -z 0, m_y, 0)$ $(-x + 1/2, 3/4, z + 1/2 0, -m_y, 0)$ |
| Mn | 4b | $(0, 0, 1/2 m_x, m_y, m_z)$ |
| | | $(1/2, 1/2, 0 m_x, -m_y, -m_z)$ |
| | | $(0, 1/2, 1/2 -m_x, m_y, -m_z)$ $(1/2, 0, 0 -m_x, -m_y, m_z)$ |
| O | 4c | $(x, 1/4, z 0, m_y, 0)$ |
| | | $(x + 1/2, 1/4, -z + 1/2 0, -m_y, 0)$ |
| | | $(-x, 3/4, -z 0, m_y, 0)$ $(-x + 1/2, 3/4, z + 1/2 0, -m_y, 0)$ |
| O | 8d | $(x, y, z m_x, m_y, m_z)$ |
| | | $(x + 1/2, -y + 1/2, -z + 1/2 m_x, -m_y, -m_z)$ |
| | | $(-x, y + 1/2, -z -m_x, m_y, -m_z)$ |
| | | $(-x + 1/2, -y, z + 1/2 -m_x, -m_y, m_z)$ |
| | | $(-x, -y, -z m_x, m_y, m_z)$ |
| | | $(-x + 1/2, y + 1/2, z + 1/2 m_x, -m_y, -m_z)$ $(x, -y + 1/2, z -m_x, m_y, -m_z)$ $(x + 1/2, y, -z + 1/2 -m_x, -m_y, m_z)$ |

TABLE II. Magnetic Wyckoff positions in $Pnma$ CaMnO_3 .

used for the reciprocal space integrations. The cutoff energy for plane waves was chosen to be 520 eV, and spin-orbit coupling was taken into account in all calculations. No DFT+U scheme was employed since both compounds prove to be insulating due to the crystal field splitting in the octahedrally coordinated Mn ion. A minimum of 300 electronic steps were considered to be a necessary condition for convergence, since the tiltings of magnetic moments may involve small energy scales.

APPENDIX D: SYMMETRY ANALYSIS OF ALTERMAGNETIC $Pnma$ PEROVSKITES

In the standard settings, the $Pnma$ perovskites with the $a^- a^- c^+$ rotation pattern has the a and c orthorhombic axes along $[\bar{1}10]$ and $[110]$ axes of the pseudocubic unit cell of the perovskite, and the orthorhombic b axis is along the $[001]$ pseudocubic direction, as shown in the figure in the main text. (Note that there is also another common setting, where the long-axis of the orthorhombic cell is the c axis, and the space group name is $Pbnm$.) In this setting, the G-AFM order on the B-site leads to a weak-ferromagnetic moment when its magnetic moments are oriented along the b or c axis, and there is no weak-ferromagnetism only when the magnetic moments of the G-AFM order is oriented along the a axis.

The magnetic space group of this configuration is $Pnma$ (#62.1.502). Note that while this space group breaks the time-reversal symmetry, it allows no macroscopic magnetic dipole moment since its point group (mmm) has three orthogonal mirror planes. However, higher order magnetic multipoles, including octupoles, are allowed, and hence this structure is purely altermagnetic.

While the presence of higher order magnetic dipoles do

not guarantee presence of induced moments on each type of atom, in $Pnma$ perovskites every atom is allowed to have magnetic moments multiple crystallographic directions. This can be best understood using the *magnetic* Wyckoff positions [71]. In Table II, we list the magnetic Wyckoff positions of each atom, along with all the sites, and the magnetic moments on those sites. The Mn atoms are on Wyckoff sites 4b, which allows magnetic moments along all three axes. This means that even though we initiate DFT calculations with magnetic moments along the a (x) axis, the moments on each Mn ion get tilted as the electronic wavefunction is updated. None of the magnetic moments are collinear with each other, but they cancel each other out perfectly due to the multiple mirror and glide planes in the space group, and hence there is no macroscopic dipole moment.

APPENDIX E: SYMMETRY ANALYSIS OF ALTERMAGNETIC MnF_2

The antiferromagnetic phase of MnF_2 [Fig. 8(a)], as well as that of RuO_2 , has the magnetic space group $P4_2'/mnm'$ (#136.5.1156). Due to the high symmetry of this simple tetragonal group, and the fact that Mn ions are placed on the intersection of multiple mirror planes, their magnetic moments are collinear even in the presence of spin-orbit coupling. This can be seen from the fact that they occupy the Wyckoff site 2a (Table III), which only allows magnetic moments along the c axis. Even though ordered magnetic moments on F ions are induced

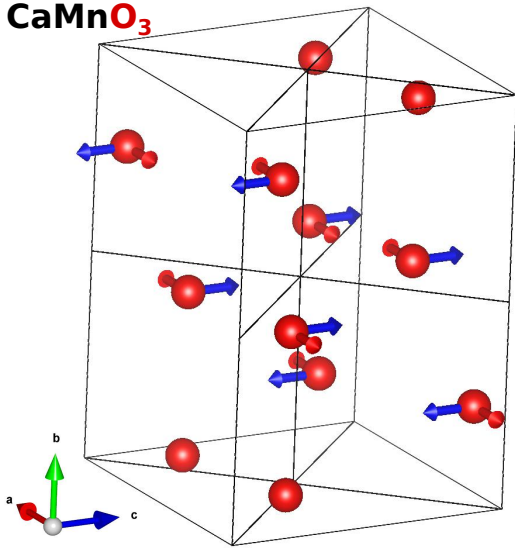


FIG. 7. Induced antiferromagnetic moments on the O ions on the 8d site in CaMnO_3 . The magnitudes of magnetic moments along a (green) and c (blue) axes are 0.02 and 0.01 Bohr magnetons respectively. The magnetic moments on the other O ions (Wyckoff letter 4c) and the Ca ions were smaller than 0.01 Bohr magneton and hence are not shown in the figure.

| | | |
|--------------------------------|----|---|
| Mn | 2a | $(0, 0, 0 0, 0, m_z)$ |
| | | $(\frac{1}{2}, \frac{1}{2}, \frac{1}{2} 0, 0, -m_z)$ |
| F | 4f | $(x, x, 0 0, 0, m_z)$ |
| | | $(-x + \frac{1}{2}, x + \frac{1}{2}, \frac{1}{2} 0, 0, -m_z)$ |
| | | $(x + \frac{1}{2}, -x + \frac{1}{2}, \frac{1}{2} 0, 0, -m_z)$ |
| | | $(-x, -x, 0 0, 0, m_z)$ |
| X | 8j | $(x, x, z m_x, m_x, m_z)$ |
| | | $(-x + \frac{1}{2}, x + \frac{1}{2}, z + \frac{1}{2} m_x, -m_x, -m_z)$ |
| | | $(x + \frac{1}{2}, -x + \frac{1}{2}, z + \frac{1}{2} -m_x, m_x, -m_z)$ |
| | | $(x + \frac{1}{2}, -x + \frac{1}{2}, -z + \frac{1}{2} m_x, -m_x, -m_z)$ |
| | | $(-x + \frac{1}{2}, x + \frac{1}{2}, -z + \frac{1}{2} -m_x, m_x, -m_z)$ |
| | | $(-x, -x, z -m_x, -m_x, m_z)$ |
| | | $(x, x, -z -m_x, -m_x, m_z)$ |
| $(-x, -x, -z m_x, m_x, m_z)$ | | |

TABLE III. Magnetic Wyckoff positions in MnF_2 with space group $P4_2'/mnm'$.

due to the magnetic order, they are also collinear since the symmetry of the 4f Wyckoff site of F does not allow any noncollinear magnetic moments either. Our first principles calculations show that the magnetic moments on the anions in MnF_2 are $\sim 0.03 \mu_B$.

Even though no noncolinear atomic moments are present in MnF_2 , this does not mean that the spin density is collinear everywhere in the unit cell. One can use the list of all Wyckoff positions of a magnetic space group, even though they are not occupied by atoms, to predict the direction of the local magnetic moments at a specific point in the unit cell, and whether they lead to different multipoles. In Table III, we list the coordinates and allowed moments of the Wyckoff site 8j, which is shown in Fig. 8(b). This unoccupied site allows noncollinear magnetic moments by symmetry, which means that in the AFM phase of MnF_2 , these points will have a nonzero and noncollinear spin density. The in-plane components of this spin density is shown in Fig. 8(c-d). This spin density does not correspond to a single multipole moment, but it is a superposition of many different moments. For example, the in-plane component of the octupole moment $M_{xyz} = \sqrt{15} (yz\hat{x} + zx\hat{y} + xy\hat{z})$ is nonzero due to the spin pattern shown in Fig. 8.

APPENDIX F: SYMMETRY-PROTECTED NODAL LINES

Let us analyze the band degeneracies in the low-energy model for AM systems. As explained in the main text, the effective Hamiltonian is given by $\mathcal{H} = \sum_{\mathbf{k}} \psi_{\mathbf{k}}^\dagger H(\mathbf{k}) \psi_{\mathbf{k}}$, where $\psi_{\mathbf{k}} = (c_{\mathbf{k}\uparrow}, c_{\mathbf{k}\downarrow})^T$ and $H(\mathbf{k}) = H_0(\mathbf{k}) + H_{\text{int}}(\mathbf{k})$ with

$$H_0(\mathbf{k}) = \varepsilon_{\mathbf{k}} \sigma^0, \quad (\text{F1})$$

$$H_{\text{int}}(\mathbf{k}) = -\lambda \mathbf{d}_{\text{eff}}(\mathbf{k}) \cdot \boldsymbol{\sigma}. \quad (\text{F2})$$

For AM order parameters that transform as 1D irreps of point groups, we have $\mathbf{d}_{\text{eff}}(\mathbf{k}) = \Phi \mathbf{d}(\mathbf{k})$ with $\mathbf{d}(\mathbf{k})$ given in Table I of the main text. In the case of multi-dimensional irreps, we define $\mathbf{d}_{\text{eff}}(\mathbf{k}) = \sum_i \Phi_0^i \mathbf{d}_i(\mathbf{k})$,

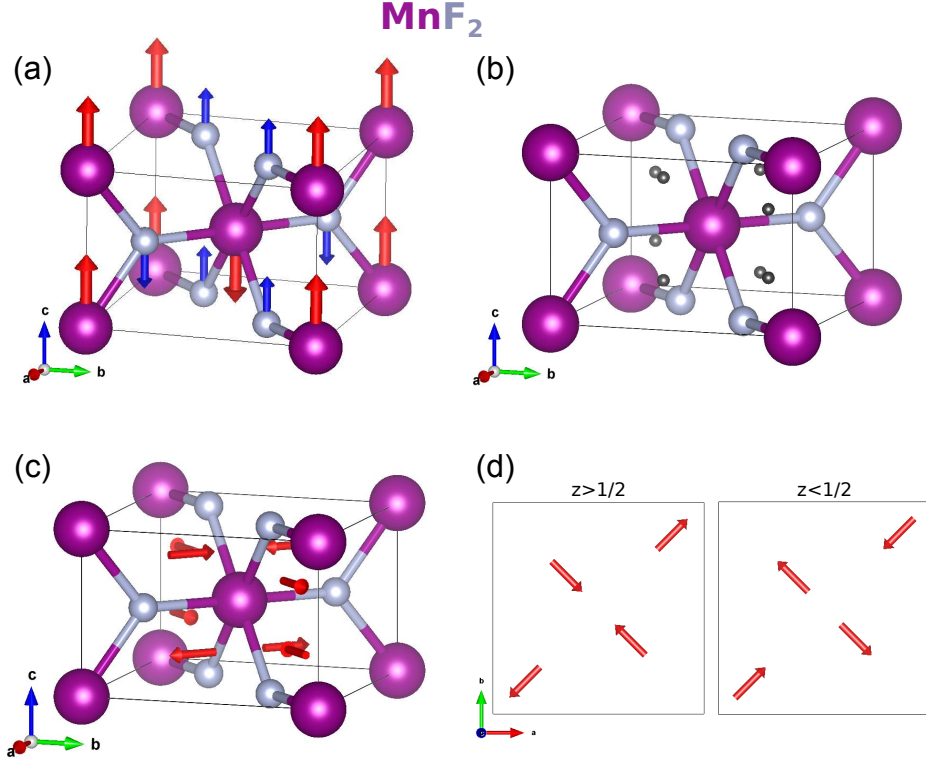


FIG. 8. (a) MnF_2 has the Rutile crystal structure, where the Mn ions (purple spheres) are in the corners and the body center of a simple-tetragonal cell. The AFM order (red arrows) do not reduce the translational symmetry, but induces magnetic moments on the F ions (blue arrows). (b) The 8j Wyckoff sites are shown as grey spheres. (c) In-plane components of the allowed magnetic moments on the 8j Wyckoff sites. (d) Same as panel (c), but from a different angle.

where Φ_0^i is the order parameter configuration that minimizes the corresponding free energy. For the 2D irreps E_{2g}^- in D_{6h} and E_g^- in O_h , as shown in Appendix B, the two-component order parameter is parametrized as in a six-state clock model:

$$(\Phi^1, \Phi^2) = (\Phi \cos(p\pi/6), \Phi \sin(p\pi/6)), \quad (\text{F3})$$

where $p \in \{0, 1, \dots, 11\}$. For the 3D irrep T_{2g}^- in O_h , we have two possible configurations, as explained in Appendix B. The first one is:

$$(\Phi^1, \Phi^2, \Phi^3) = (\Phi \delta_{q1}, \Phi \delta_{q2}, \Phi \delta_{q3}), \quad q \in \{1, 2, 3\}, \quad (\text{F4})$$

whereas the second one is given by

$$(\Phi^1, \Phi^2, \Phi^3) = \Phi (\zeta_1, \zeta_2, \zeta_3), \quad (\text{F5})$$

where $\zeta_i = \pm 1$ and $\zeta_1 \zeta_2 \zeta_3 = 1$.

Assuming a “pure” AM state, which has zero net magnetization, the components of $\mathbf{d}_{\text{eff}}(\mathbf{k})$ are homogeneous functions of \mathbf{k} . The conditions $d_{\text{eff},\mu}(\mathbf{k}) = 0$ for each component $\mu \in \{x, y, z\}$ define sets of planes that contain $\mathbf{k} = 0$ as well as some high-symmetry directions in reciprocal space. The band touching (i.e. nodes of the Zeeman splitting) occurs when all three components of

$\mathbf{d}_{\text{eff}}(\mathbf{k})$ vanish simultaneously. We denote the nodal lines as follows (here $\alpha \neq \beta \neq \gamma \in \{x, y, z\}$):

$$\mathcal{L}_\alpha : k_\beta = 0 \quad \forall \beta \neq \alpha, \quad (\text{F6})$$

$$\mathcal{L}_{\alpha\beta} : k_\alpha = k_\beta, \quad k_\gamma = 0, \quad (\text{F7})$$

$$\mathcal{L}_{\alpha\bar{\beta}} : k_\alpha = -k_\beta, \quad k_\gamma = 0, \quad (\text{F8})$$

$$\mathcal{L}_{6a} : k_y = \sqrt{3}k_x, \quad k_z = 0, \quad (\text{F9})$$

$$\mathcal{L}_{\bar{6}a} : k_y = -\sqrt{3}k_x, \quad k_z = 0, \quad (\text{F10})$$

$$\mathcal{L}_{6b} : k_y = k_x/\sqrt{3}, \quad k_z = 0, \quad (\text{F11})$$

$$\mathcal{L}_{\bar{6}b} : k_y = -k_x/\sqrt{3}, \quad k_z = 0, \quad (\text{F12})$$

$$\mathcal{L}_{6c} : k_y = (2 + \sqrt{3})k_x, \quad k_z = 0, \quad (\text{F13})$$

$$\mathcal{L}_{\bar{6}c} : k_y = -(2 + \sqrt{3})k_x, \quad k_z = 0, \quad (\text{F14})$$

$$\mathcal{L}_{6d} : k_y = (2 - \sqrt{3})k_x, \quad k_z = 0, \quad (\text{F15})$$

$$\mathcal{L}_{\bar{6}d} : k_y = -(2 - \sqrt{3})k_x, \quad k_z = 0. \quad (\text{F16})$$

In the case of multi-dimensional irreps, the vector $\mathbf{d}_{\text{eff}}(\mathbf{k})$ may also display nodal planes, which we denote as

$$\mathcal{P}_\alpha : k_\alpha = 0. \quad (\text{F17})$$

In Table IV we show the nodal manifolds for the irreps of the crystallographic point groups investigated in this

TABLE IV. Nodal lines and planes in the spectrum of the effective Hamiltonian with AM order parameter transforming as the irreps of crystallographic point groups D_{2h} , D_{4h} , D_{6h} , and O_h . In the columns associated with the nodal lines, as defined in Eqs. (F6)-(F16), the number 1 (2) indicates that \mathcal{L} is a nodal line with Berry phase $\pm\pi$ ($\pm 2\pi$) for the irrep in the corresponding row. All nodal lines belong to at least one mirror plane of the point group. The check marks in the last three columns indicate that \mathcal{P}_α is a nodal plane, in which case the lines contained in that plane are not counted as nodal lines. Note that the nodal lines for the irrep T_{2g}^- with the configuration specified by Eq. (F5) refer here to the case $\eta = 1$.

| Group | Irrep | \mathcal{L}_x | \mathcal{L}_y | \mathcal{L}_z | \mathcal{L}_{xy} | $\mathcal{L}_{\bar{x}\bar{y}}$ | \mathcal{L}_{yz} | $\mathcal{L}_{y\bar{z}}$ | \mathcal{L}_{xz} | $\mathcal{L}_{\bar{x}\bar{z}}$ | \mathcal{L}_{6a} | $\mathcal{L}_{\bar{6}a}$ | \mathcal{L}_{6b} | $\mathcal{L}_{\bar{6}b}$ | \mathcal{L}_{6c} | $\mathcal{L}_{\bar{6}c}$ | \mathcal{L}_{6d} | $\mathcal{L}_{\bar{6}d}$ | \mathcal{P}_x | \mathcal{P}_y | \mathcal{P}_z |
|----------|---------------------------------|-----------------|-----------------|-----------------|--------------------|--------------------------------|--------------------|--------------------------|--------------------|--------------------------------|--------------------|--------------------------|--------------------|--------------------------|--------------------|--------------------------|--------------------|--------------------------|-----------------|-----------------|-----------------|
| D_{2h} | A_{1g}^- | 1 | 1 | 1 | | | | | | | | | | | | | | | | | |
| D_{4h} | A_{1g}^- | 1 | 1 | 1 | 1 | 1 | | | | | | | | | | | | | | | |
| D_{4h} | B_{1g}^- | 1 | 1 | 1 | | | | | | | | | | | | | | | | | |
| D_{4h} | B_{2g}^- | | | 1 | 1 | 1 | | | | | | | | | | | | | | | |
| D_{6h} | A_{1g}^- | 1 | 1 | 1 | | | | | | | 1 | 1 | 1 | 1 | | | | | | | |
| D_{6h} | B_{1g}^- | | | 2 | | | | | | | | | | | | | | | | | |
| D_{6h} | B_{2g}^- | | | 2 | | | | | | | | | | | | | | | | | |
| D_{6h} | $E_{2g}^- (p = 0, 6)$ | 1 | 1 | 1 | | | | | | | | | | | | | | | | | |
| D_{6h} | $E_{2g}^- (p = 1, 7)$ | | | 1 | | | | | | | | | | | 1 | | | 1 | | | |
| D_{6h} | $E_{2g}^- (p = 2, 8)$ | | | 1 | | | | | | 1 | | | | 1 | | | | | | | |
| D_{6h} | $E_{2g}^- (p = 3, 9)$ | | | 1 | 1 | 1 | | | | | | | | | | | | | | | |
| D_{6h} | $E_{2g}^- (p = 4, 10)$ | | | 1 | | | | | | | 1 | 1 | | | | | | | | | |
| D_{6h} | $E_{2g}^- (p = 5, 11)$ | | | 1 | | | | | | | | | | | 1 | 1 | | | | | |
| O_h | A_{1g}^- | 1 | 1 | 1 | 1 | 1 | 1 | 1 | 1 | 1 | | | | | | | | | | | |
| O_h | A_{2g}^- | 1 | 1 | 1 | | | | | | | | | | | | | | | | | |
| O_h | $E_g^- (p = 0, 6)$ | | | 1 | | | | | | | | | | | | | | | | | ✓ |
| O_h | $E_g^- (p = 2, 8)$ | 1 | | | | | | | | | | | | | | | | | | ✓ | |
| O_h | $E_g^- (p = 4, 10)$ | | 1 | | | | | | | | | | | | | | | | | ✓ | |
| O_h | $E_g^- (p = 1, 3, 5, 7, 9, 11)$ | 1 | 1 | 1 | | | | | | | | | | | | | | | | | |
| O_h | $T_{2g}^- (q = 1)$ | | | 1 | 1 | 1 | | | | | | | | | | | | | | | |
| O_h | $T_{2g}^- (q = 2)$ | 1 | | | | | 1 | 1 | | | | | | | | | | | | | |
| O_h | $T_{2g}^- (q = 3)$ | | 1 | | | | | | 1 | 1 | | | | | | | | | | | |
| O_h | $T_{2g}^- [(1, 1, 1)]$ | | | | 1 | | 1 | | 1 | | | | | | | | | | | | |
| O_h | $T_{2g}^- [(1, -1, -1)]$ | | | | 1 | | | 1 | | 1 | | | | | | | | | | | |
| O_h | $T_{2g}^- [(-1, 1, -1)]$ | | | | | 1 | 1 | | | 1 | | | | | | | | | | | |
| O_h | $T_{2g}^- [(-1, -1, 1)]$ | | | | | 1 | | 1 | 1 | | | | | | | | | | | | |

work. For each nodal line, we compute the Berry phase

$$\gamma_{\pm} = \oint d\mathbf{k} \cdot \mathbf{A}_{\pm}(\mathbf{k}), \quad (\text{F18})$$

where $\mathbf{A}_{\lambda}(\mathbf{k}) = i\langle u_{\lambda}(\mathbf{k}) | \nabla_{\mathbf{k}} | u_{\lambda}(\mathbf{k}) \rangle$ is the Berry connection, calculated from the eigenvectors of the Hamiltonian in the upper ($\lambda = +$) or lower ($\lambda = -$) band, and the integration path encircles the nodal line. On general grounds, we expect topologically trivial nodal lines ($\gamma_{\pm} = 0$) to be unstable against perturbations.

More precisely, we can analyze the stability of the AM phase using the classification of gapless topological phases [35, 52, 72]. The band touching in the spectrum of $H(\mathbf{k})$ is governed by the Fermi “surface” (point, line) of $H_{\text{int}}(\mathbf{k})$. In all cases considered in this work, $H_{\text{int}}(\mathbf{k})$ breaks time-reversal symmetry because $\mathbf{d}_{\text{eff}}(\mathbf{k})$ is an even function of momentum and time reversal acts in spin space as $\boldsymbol{\sigma} \mapsto -\boldsymbol{\sigma}$. However, $H_{\text{int}}(\mathbf{k})$ exhibits a charge conjugation symmetry

$$\mathcal{C} : C^{-1} H_{\text{int}}(-\mathbf{k}) C = -H_{\text{int}}(\mathbf{k}), \quad (\text{F19})$$

with $C = \mathcal{K}\sigma^y$, where \mathcal{K} denotes complex conjugation. Since $C^2 = -1$, the AM models belong to class C in

the periodic table of topological phases [72]. The nodal lines correspond to Fermi “surfaces” of codimension 2, whose stability requires mirror symmetries [35]. A mirror symmetry with respect to the plane that contains $\mathbf{k} = 0$ and is perpendicular to unit vector $\hat{\mathbf{n}}$ is defined by the condition

$$R_{\hat{\mathbf{n}}} H_{\text{int}}(\mathcal{R}_{\hat{\mathbf{n}}}\mathbf{k}) R_{\hat{\mathbf{n}}} = H_{\text{int}}(\mathbf{k}), \quad (\text{F20})$$

where $R_{\hat{\mathbf{n}}} = \boldsymbol{\sigma} \cdot \hat{\mathbf{n}} = R_{\hat{\mathbf{n}}}^{-1}$ and $\mathcal{R}_{\hat{\mathbf{n}}}\mathbf{k} = -(\mathbf{k} \cdot \hat{\mathbf{n}})\hat{\mathbf{n}} + (\hat{\mathbf{n}} \times \mathbf{k}) \times \hat{\mathbf{n}}$. If \mathbf{k} belongs to the mirror plane, $\mathbf{k} \cdot \hat{\mathbf{n}} = 0$, then $H_{\text{int}}(\mathbf{k})$ is invariant under the reflection, and the spin component in the direction of $\hat{\mathbf{n}}$ becomes a good quantum number. All nodal lines listed in Table IV belong to at least one mirror plane.

The perturbation of interest here is the Zeeman term

$$H_Z = g_s \mu_B \mathbf{h} \cdot \boldsymbol{\sigma}. \quad (\text{F21})$$

Note that H_Z respects the charge conjugation symmetry. Mirror symmetry imposes that the magnetic field must be perpendicular to the mirror plane, $\mathbf{h} = h\hat{\mathbf{n}}$. Importantly, the reflection operator $R_{\hat{\mathbf{n}}}$ anticommutes with

C. In this case, for $h \neq 0$ the nodal lines move away from high-symmetry directions and can be protected by a $2M\mathbb{Z}$ invariant [35]. The latter can be defined as the difference in the eigenvalue of $\boldsymbol{\sigma} \cdot \hat{\mathbf{n}}$ for a fixed band as we vary \mathbf{k} across the nodal line in the mirror plane. We obtain a stable AM state when the eigenvalue of $\boldsymbol{\sigma} \cdot \hat{\mathbf{n}}$ changes sign with a nontrivial even-parity pattern. This rule generalizes the behavior of the spin polarization for collinear altermagnets [2, 3]. In addition, we have verified that symmetry-protected nodal lines are always associated with Berry phase $\pm\pi$ (denoted as 1 in Table IV). In the following we discuss some illustrative examples in detail. We also address the cases of nodal lines with Berry phase $\pm 2\pi$ and nodal planes.

1. AM model with D_{4h} point-group symmetry: B_{1g}^- irrep

We begin with the effective Hamiltonian for the AM order parameter that transforms as the B_{1g}^- irrep in the D_{4h} point group:

$$H(\mathbf{k}) = \varepsilon_{\mathbf{k}}\sigma^0 - \lambda\Phi k_y k_z \sigma^x - \lambda\Phi k_x k_z \sigma^y - \lambda\Phi\eta k_x k_y \sigma^z. \quad (\text{F22})$$

Clearly, the spectrum has three nodal lines, \mathcal{L}_x , \mathcal{L}_y , and \mathcal{L}_z . There are three mirror planes, corresponding to $\hat{\mathbf{n}} = \hat{\mathbf{x}}, \hat{\mathbf{y}}, \hat{\mathbf{z}}$. If we apply a magnetic field along an arbitrary direction, all nodal lines are gapped out. To preserve the band touching, the magnetic field must point along the [100], [010], or [001] axes. Consider, for instance, $\mathbf{h} = h\hat{\mathbf{z}}$. In this case, we obtain

$$H(\mathbf{k}) + H_Z = \varepsilon_{\mathbf{k}}\sigma^0 - \lambda\Phi k_y k_z \sigma^x - \lambda\Phi k_x k_z \sigma^y - (\lambda\Phi\eta k_x k_y - g_s\mu_B h)\sigma^z. \quad (\text{F23})$$

We see that the interacting part of the Hamiltonian no longer vanishes when we set $k_x = k_y = 0$, meaning that the degeneracy along the \mathcal{L}_z line is lifted for $h \neq 0$. However, we still obtain a degenerate spectrum for

$$k_z = 0, \quad k_x k_y = \frac{g_s\mu_B h}{\lambda\Phi\eta}. \quad (\text{F24})$$

For $h \neq 0$, the above equations define two hyperbolic nodal lines contained in the mirror plane $k_z = 0$. Within this plane, the Hamiltonian reduces to

$$H(k_x, k_y, k_z = 0) + H_Z = \varepsilon_{\mathbf{k}}\sigma^0 - (\lambda\Phi\eta k_x k_y - g_s\mu_B h)\sigma^z. \quad (\text{F25})$$

As a result, the spin polarization in the z direction becomes a good quantum number. The eigenvalue of σ^z in the lower-energy band is given by $\text{sgn}(\lambda\Phi\eta k_x k_y - g_s\mu_B h)$, changing from ± 1 to ∓ 1 as the in-plane momentum crosses the nodal lines.

The two Fermi surfaces of the AM metal touch at four pinch points where the nodal lines in Eq. (F24) cross the sphere $\varepsilon_{\mathbf{k}} = \varepsilon_F$, where ε_F is the Fermi energy. If we take the projection of the Fermi surfaces on the mirror plane $k_z = 0$, the spin polarization changes sign at

the pinch points. Note that the vicinity of the pinch points governs the low-energy excitations that involve a spin flip. Assuming an isotropic free-electron dispersion $\varepsilon_{\mathbf{k}} = k^2/(2m)$, we can calculate the critical value of the magnetic field h_c^* at which the pinch points annihilate each other. For the field along the $\hat{\mathbf{z}}$ direction, we obtain

$$h_c^* = \frac{\lambda\Phi k_F^2}{2g_s\mu_B}, \quad (\text{F26})$$

where $k_F = \sqrt{2m\varepsilon_F}$ is the Fermi momentum. For $|h| > h_c^*$, the nodal lines do not intercept the Fermi sphere, and the system has disconnected Fermi surfaces.

In the limit $|h| \ll h_c^*$, we can treat the Zeeman term as a small perturbation and expand the Hamiltonian around the pinch points with $|\mathbf{k}| = k_F$. Consider, for instance, the vicinity of the pinch point on the positive x -axis, with $\mathbf{k} = (k_F + q_x)\hat{\mathbf{x}} + q_y\hat{\mathbf{y}} + q_z\hat{\mathbf{z}}$, where $|q| \ll k_F$. To first order in \mathbf{q} , we obtain

$$H(\mathbf{k}) + H_Z \approx \varepsilon_F + v_F q_x \sigma^0 - \lambda\Phi k_F q_z \sigma^y - (\lambda\Phi\eta k_F q_y - g_s\mu_B h)\sigma^z, \quad (\text{F27})$$

where $v_F = k_F/m$. The corresponding dispersion reads

$$\varepsilon_{\mathbf{k}} \approx \varepsilon_F + v_F q_x \pm \sqrt{(\lambda\Phi k_F q_z)^2 + (\lambda\Phi\eta k_F q_y - g_s\mu_B h)^2}. \quad (\text{F28})$$

This result is reminiscent of the spectrum of type-II Weyl semimetals, which exhibit touching points between electron and hole Fermi pockets [36]. Note, however, that here we have a nodal line, which for $h = 0$ runs along the k_x axis. To leading order in h , the node (pinch point) remains in the $k_z = 0$ plane, but moves in the direction perpendicular to the k_x axis to $q_y = (h/h_c^*)k_F/2$. By taking a cut in momentum space at fixed $q_x = 0$, one can see that Eq. (F27) is equivalent to a Dirac Hamiltonian, which accounts for the Berry phase $\pm\pi$ for a path that winds around the nodal line.

2. AM model with D_{4h} point-group symmetry: A_{1g}^- irrep

The effective Hamiltonian in this case reads

$$H(\mathbf{k}) = \varepsilon_{\mathbf{k}}\sigma^0 - \lambda\Phi k_y k_z \sigma^x + \lambda\Phi k_x k_z \sigma^y - \lambda\Phi\eta k_x k_y (k_x^2 - k_y^2)\sigma^z. \quad (\text{F29})$$

As listed in Table IV, there are five nodal lines in total, all of which are associated with Berry phase $\pm\pi$. In the absence of a magnetic field, the Fermi surfaces touch at 10 pinch points; see Fig. 9(a). Upon applying a magnetic field in the z direction, the \mathcal{L}_z line is gapped out, but the nodal lines in the $k_z = 0$ mirror plane persist and are given by the equations

$$k_z = 0, \quad k_x k_y (k_x^2 - k_y^2) = \frac{g_s\mu_B h}{\lambda\Phi\eta}. \quad (\text{F30})$$

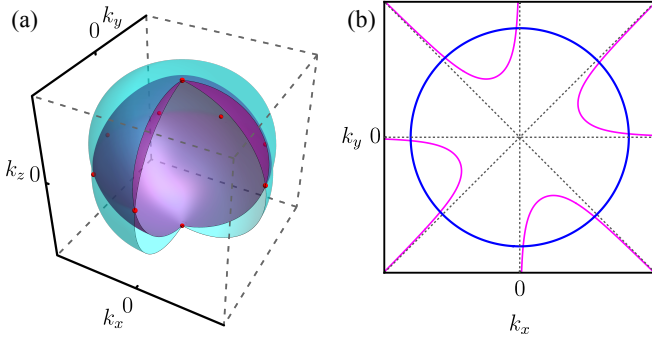


FIG. 9. AM state whose order parameter transforms as the A_{1g}^- irrep of the D_{4h} group. (a) Fermi surfaces showing 9 out of 10 pinch points (red dots); to aid visualization, we omit the domain where $k_x > 0$ and $k_y < 0$. (b) Nodal lines in the $k_z = 0$ plane for $\mathbf{h} = 0$ (dashed lines) and $\mathbf{h} = h\hat{\mathbf{z}}$ with $h > 0$ (solid magenta lines). The blue circle represents the projection of the noninteracting Fermi surface $|\mathbf{k}| = k_F$. The intersection of the nodal lines with the circle determine the location of the pinch points in the AM phase.

The nodal lines for $h \geq 0$ are depicted in Fig. 9(b). Within the $k_z = 0$ plane, the Hamiltonian reduces to

$$H(k_x, k_y, k_z = 0) + H_Z = \varepsilon_{\mathbf{k}}\sigma^0 - [\lambda\Phi\eta k_x k_y (k_x^2 - k_y^2) - g\mu_s h]\sigma^z. \quad (\text{F31})$$

In the AM phase, the spin polarization changes sign 8 times as \mathbf{k} is varied around one of the Fermi surfaces in the mirror plane, corresponding to a g -wave pattern. The critical magnetic field along the $\hat{\mathbf{z}}$ direction is

$$h_c^* = \frac{\lambda\Phi\eta k_F^4}{4g_s\mu_B} \quad (\mathbf{h} \parallel \hat{\mathbf{z}}). \quad (\text{F32})$$

On the other hand, if we apply the magnetic field along the $\hat{\mathbf{x}}$ axis, the AM state has two stable nodal lines in the $k_x = 0$ plane, given by

$$k_x = 0, \quad k_y k_z = \frac{g_s\mu_B h}{\lambda\Phi}. \quad (\text{F33})$$

In this case, the critical magnetic field is

$$h_c^* = \frac{\lambda\Phi k_F^2}{2g_s\mu_B} \quad (\mathbf{h} \parallel \hat{\mathbf{x}}). \quad (\text{F34})$$

3. AM model with D_{6h} point-group symmetry: B_{1g}^- irrep

According to Table IV, the B_{1g}^- and B_{2g}^- irreps in the D_{6h} group are peculiar because in these cases there is only one nodal line with Berry phase $\pm 2\pi$. Let us consider the B_{1g}^- irrep. Similar results hold for B_{2g}^- upon exchanging the roles of $\hat{\mathbf{x}}$ and $\hat{\mathbf{y}}$ directions. The effective Hamiltonian is

$$H(\mathbf{k}) = \varepsilon_{\mathbf{k}}\sigma^0 - \lambda\Phi(k_x^2 - k_y^2)\sigma^x + 2\lambda\Phi k_x k_y \sigma^y - \lambda\Phi\eta k_x k_z (k_x^2 - 3k_y^2)\sigma^z. \quad (\text{F35})$$

Let us consider the vicinity of the \mathcal{L}_z line. Expanding the Hamiltonian for $\mathbf{k} = (q_x, q_y, k_F + q_z)$ to leading order in \mathbf{q} , we obtain

$$H(\mathbf{k}) \approx \varepsilon_F\sigma^0 - \lambda\Phi(q_x^2 - q_y^2)\sigma^x + 2\lambda\Phi q_x q_y \sigma^y, \quad (\text{F36})$$

where we drop the $\mathcal{O}(|\mathbf{q}|^3)$ terms multiplying σ^z . This Hamiltonian describes a double-Weyl node with C_6 symmetry [37], hence the Berry phase $\pm 2\pi$. Unlike the Dirac Hamiltonian for nodal lines with Berry phase $\pm\pi$, cf. Eq. (F27), in this case the band splitting scales quadratically with momentum in the direction perpendicular to the nodal line.

The \mathcal{L}_z line belongs to the mirror plane $k_x = 0$. Adding a Zeeman term with $\mathbf{h} = h\hat{\mathbf{x}}$, we obtain the Hamiltonian in the mirror plane

$$H(k_x = 0, k_y, k_z) = \varepsilon_{\mathbf{k}}\sigma^0 + (\lambda\Phi k_y^2 + g_s\mu_B h)\sigma^x. \quad (\text{F37})$$

Note that for $h = 0$ the eigenvalue of σ^x does not change sign in the mirror plane. As a consequence, the nodal line is not protected by the mirror symmetry. Furthermore, the magnetic field breaks the C_6 symmetry of the nodal line, destabilizing the double-Weyl node. The outcome depends on the sign of h . For $h > 0$, the nodal line is gapped out, but there appear two Weyl points off the mirror plane, located at

$$k_x = \pm \sqrt{\frac{g_s\mu_B h}{\lambda\Phi}}, \quad k_y = k_z = 0. \quad (\text{F38})$$

In this case, finding the band touching at the Fermi level requires fine tuning. In contrast, for $h < 0$ the nodal line splits into two lines given by

$$k_x = 0, \quad k_y = \pm \sqrt{\frac{g_s\mu_B |h|}{\lambda\Phi}}. \quad (\text{F39})$$

Note that the two lines remain in the mirror plane, but move off the high-symmetry k_z axis. One can check that, after they split, each line carries a Berry phase $\pm\pi$. Moreover, for $h < 0$ the eigenvalue of σ^x changes sign across the nodal lines. As a result, we find that for $h < 0$ the AM state with four pinch points at the Fermi surface remains stable up to a critical value of the field

$$|h_c^*| = \frac{\lambda\Phi k_F^2}{g_s\mu_B}. \quad (\text{F40})$$

4. AM model with D_{6h} point-group symmetry: E_{2g}^- irrep

We now turn to multi-dimensional irreps, starting with the E_{2g}^- irrep in the D_{6h} point group. The effective Hamiltonian for the two-component AM order parameter

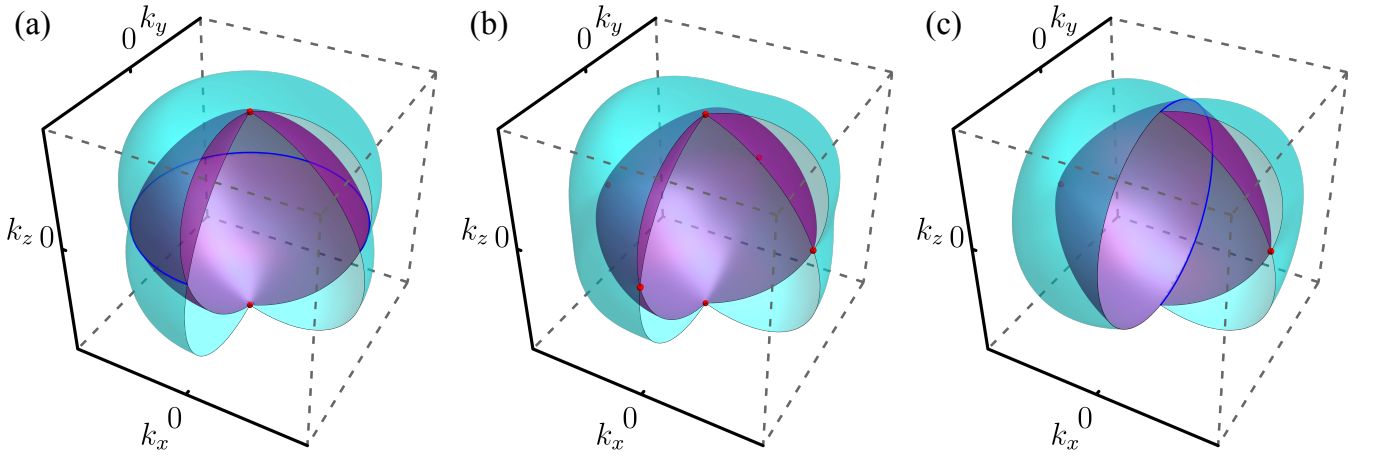


FIG. 10. Fermi surfaces for the AM state whose order parameter transforms as the E_g^- irrep of the O_h group; see Eq. (F44). (a) With the six-state-clock index set to $p = 0$, the Fermi surfaces touch at two pinch points associated with the \mathcal{L}_z nodal line and along a line contained in the \mathcal{P}_z nodal plane. (b) For $p = 1$, the spectrum contains three nodal lines, and the Fermi surfaces touch at 6 pinch points. (c) The case of $p = 2$ is similar to $p = 0$, but with Fermi surface touching governed by the \mathcal{L}_x nodal line and the \mathcal{P}_x nodal plane.

in Eq. (F3) is

$$\begin{aligned}
 H(\mathbf{k}) = & \varepsilon_{\mathbf{k}}\sigma^0 - \lambda\Phi \left[\cos\left(\frac{p\pi}{6}\right)k_y + \sin\left(\frac{p\pi}{6}\right)k_x \right] k_z\sigma^x \\
 & - \lambda\Phi \left[\cos\left(\frac{p\pi}{6}\right)k_x - \sin\left(\frac{p\pi}{6}\right)k_y \right] k_z\sigma^y \\
 & - \lambda\Phi\eta \left[2\cos\left(\frac{p\pi}{6}\right)k_xk_y + \sin\left(\frac{p\pi}{6}\right)(k_x^2 - k_y^2) \right] \sigma^z.
 \end{aligned} \tag{F41}$$

The location of the nodal lines varies with $p \in \{0, 1, \dots, 11\}$ as given in Table IV. The mirror planes correspond to $\hat{\mathbf{n}} = \hat{\mathbf{z}}$ and $\hat{\mathbf{n}} = \cos\theta_p\hat{\mathbf{x}} + \sin\theta_p\hat{\mathbf{y}}$ with $\theta_p = (6-p)\pi/12$. Applying a magnetic field in the $\hat{\mathbf{z}}$ direction, we find that the nodal lines in the $k_z = 0$ plane are given by

$$\begin{aligned}
 k_z &= 0, \\
 2\cos\left(\frac{p\pi}{6}\right)k_xk_y + \sin\left(\frac{p\pi}{6}\right)(k_x^2 - k_y^2) &= \frac{g_s\mu_B\hbar}{\lambda\Phi\eta}.
 \end{aligned} \tag{F42}$$

For all values of p , there are two stable nodal lines in the mirror plane. The eigenvalue of σ^z changes sign across the nodal lines, and the behavior is similar to the previous examples with Berry phase $\pm\pi$.

5. AM Model with O_h point-group symmetry: E_g^- irrep

As an example of an AM model exhibiting nodal planes, we consider the E_g^- irrep in the O_h point group,

with effective Hamiltonian

$$\begin{aligned}
 H(\mathbf{k}) = & \varepsilon_{\mathbf{k}}\sigma^0 - \lambda\Phi \left[\sqrt{3}\cos\left(\frac{p\pi}{6}\right) - \sin\left(\frac{p\pi}{6}\right) \right] k_yk_z\sigma^x \\
 & + \lambda\Phi \left[\sqrt{3}\cos\left(\frac{p\pi}{6}\right) + \sin\left(\frac{p\pi}{6}\right) \right] k_xk_z\sigma^y \\
 & - 2\lambda\Phi\sin\left(\frac{p\pi}{6}\right)k_xk_y\sigma^z,
 \end{aligned} \tag{F44}$$

where $p \in \{0, 1, \dots, 11\}$. The mirror planes correspond to $\hat{\mathbf{n}} = \hat{\mathbf{x}}, \hat{\mathbf{y}}, \hat{\mathbf{z}}$. For odd values of p , the spectrum contains three nodal lines along the crystallographic axes, and the discussion is similar to the other examples of nodal lines with Berry phase $\pm\pi$. For even values of p , the nodal manifolds include a line and the plane perpendicular to it; see Table IV. As a result, in the absence of a magnetic field the Fermi surfaces touch at two pinch points and along a line contained in the nodal plane, as shown in Fig. 10.

To analyze the effects of a magnetic field, let us focus on the Hamiltonian for $p = 0$:

$$H(\mathbf{k}) = \varepsilon_{\mathbf{k}}\sigma^0 - \sqrt{3}\lambda\Phi k_yk_z\sigma^x + \sqrt{3}\lambda\Phi k_xk_z\sigma^y. \tag{F45}$$

Clearly, adding a magnetic field along the $\hat{\mathbf{z}}$ direction lifts the band degeneracy, as the \mathcal{L}_z nodal line is not protected by the mirror symmetry about the $k_z = 0$ plane and nodal planes (codimension 1) in class C are topologically trivial and hence unstable [35]. On the other hand, for a magnetic field along the $\hat{\mathbf{x}}$ direction we are left with two nodal lines in the $k_x = 0$ plane:

$$k_x = 0, \quad k_yk_z = \frac{g_s\mu_B\hbar}{\sqrt{3}\lambda\Phi}. \tag{F46}$$

A similar result holds for a field along the $\hat{\mathbf{y}}$ direction. We conclude that a magnetic field that respects a mirror symmetry and whose direction is contained in the nodal

plane turns the nodal plane and the nodal line present at $h = 0$ into a pair of nodal lines within the mirror plane.

After the nodal plane is removed for $h \neq 0$, the pair of nodal lines in the AM state behaves as in the standard cases.

-
- [1] L. Šmejkal, R. González-Hernández, T. Jungwirth, and J. Sinova, Crystal time-reversal symmetry breaking and spontaneous Hall effect in collinear antiferromagnets, *Sci. Adv.* **6**, eaaz8809 (2020).
- [2] L. Šmejkal, J. Sinova, and T. Jungwirth, Beyond Conventional Ferromagnetism and Antiferromagnetism: A Phase with Nonrelativistic Spin and Crystal Rotation Symmetry, *Phys. Rev. X* **12**, 031042 (2022).
- [3] L. Šmejkal, J. Sinova, and T. Jungwirth, Emerging Research Landscape of Altermagnetism, *Phys. Rev. X* **12**, 040501 (2022).
- [4] I. Turek, Altermagnetism and magnetic groups with pseudoscalar electron spin, *Phys. Rev. B* **106**, 094432 (2022).
- [5] I. I. Mazin, K. Koepf, M. D. Johannes, R. González-Hernández, and L. Šmejkal, Prediction of unconventional magnetism in doped FeSb₂, *Proc. Natl. Acad. Sci. U.S.A.* **118**, e2108924118 (2021).
- [6] Z. Feng, X. Zhou, L. Šmejkal, L. Wu, Z. Zhu, H. Guo, R. González-Hernández, X. Wang, H. Yan, P. Qin, *et al.*, An anomalous Hall effect in altermagnetic ruthenium dioxide, *Nat. Electron.* **5**, 735 (2022).
- [7] R. D. Gonzalez Betancourt, J. Zubáč, R. Gonzalez-Hernandez, K. Geishendorf, Z. Šobáň, G. Springholz, K. Olejník, L. Šmejkal, J. Sinova, T. Jungwirth, S. T. B. Goennenwein, A. Thomas, H. Reichlová, J. Železný, and D. Kriegner, Spontaneous Anomalous Hall Effect Arising from an Unconventional Compensated Magnetic Phase in a Semiconductor, *Phys. Rev. Lett.* **130**, 036702 (2023).
- [8] I. I. Mazin, Altermagnetism in MnTe: Origin, predicted manifestations, and routes to detwinning, *Phys. Rev. B* **107**, L100418 (2023).
- [9] H. Bai, Y. C. Zhang, Y. J. Zhou, P. Chen, C. H. Wan, L. Han, W. X. Zhu, S. X. Liang, Y. C. Su, X. F. Han, F. Pan, and C. Song, Efficient Spin-to-Charge Conversion via Altermagnetic Spin Splitting Effect in Antiferromagnet RuO₂, *Phys. Rev. Lett.* **130**, 216701 (2023).
- [10] T. Aoyama and K. Ohgushi, Piezomagnetic Properties in Altermagnetic MnTe, [arXiv:2305.14786](https://arxiv.org/abs/2305.14786) (2023).
- [11] Y. Guo, H. Liu, O. Janson, I. C. Fulga, J. van den Brink, and J. I. Facio, Spin-split collinear antiferromagnets: A large-scale ab-initio study, *Mater. Today Phys.* **32**, 100991 (2023).
- [12] G. Cuono, R. M. Sattigeri, S. J., and C. Autieri, Orbital-selective altermagnetism and correlation-enhanced spin-splitting in transition metal oxides, [arXiv:2306.17497](https://arxiv.org/abs/2306.17497) (2023).
- [13] T. A. Maier and S. Okamoto, Weak-Coupling Theory of Neutron Scattering as a Probe of Altermagnetism, [arXiv:2307.03793](https://arxiv.org/abs/2307.03793) (2023).
- [14] C. R. Steward, R. M. Fernandes, and J. Schmalian, Dynamic paramagnon-polarons in altermagnets, [arXiv:2307.01855](https://arxiv.org/abs/2307.01855) (2023).
- [15] S. Hayami, Y. Yanagi, and H. Kusunose, Momentum-Dependent Spin Splitting by Collinear Antiferromagnetic Ordering, *J. Phys. Soc. Jpn.* **88**, 123702 (2019).
- [16] K.-H. Ahn, A. Hariki, K.-W. Lee, and J. Kuneš, Antiferromagnetism in RuO₂ as *d*-wave Pomeranchuk instability, *Phys. Rev. B* **99**, 184432 (2019).
- [17] L.-D. Yuan, Z. Wang, J.-W. Luo, E. I. Rashba, and A. Zunger, Giant momentum-dependent spin splitting in centrosymmetric low-*Z* antiferromagnets, *Phys. Rev. B* **102**, 014422 (2020).
- [18] L.-D. Yuan and A. Zunger, Degeneracy removal of spin bands in antiferromagnets with non-interconvertible spin motif pair, [arXiv:2211.07803](https://arxiv.org/abs/2211.07803) (2022).
- [19] S. Bhowal and N. A. Spaldin, Magnetic octupoles as the order parameter for unconventional antiferromagnetism, [arXiv:2212.03756](https://arxiv.org/abs/2212.03756) (2022).
- [20] I. Pomeranchuk, On the stability of a Fermi liquid, *Sov. Phys. JETP* **8**, 361 (1958).
- [21] C. Wu, K. Sun, E. Fradkin, and S.-C. Zhang, Fermi liquid instabilities in the spin channel, *Phys. Rev. B* **75**, 115103 (2007).
- [22] V. Oganesyan, S. A. Kivelson, and E. Fradkin, Quantum theory of a nematic Fermi fluid, *Phys. Rev. B* **64**, 195109 (2001).
- [23] S. Hayami, M. Yatsushiro, Y. Yanagi, and H. Kusunose, Classification of atomic-scale multipoles under crystallographic point groups and application to linear response tensors, *Phys. Rev. B* **98**, 165110 (2018).
- [24] R. Winkler and U. Zülicke, Theory of electric, magnetic, and toroidal polarizations in crystalline solids with applications to hexagonal lonsdaleite and cubic diamond, *Phys. Rev. B* **107**, 155201 (2023).
- [25] D. Fiore Mosca, L. V. Pourovskii, and C. Franchini, Modeling magnetic multipolar phases in density functional theory, *Phys. Rev. B* **106**, 035127 (2022).
- [26] C. Ederer and N. A. Spaldin, Towards a microscopic theory of toroidal moments in bulk periodic crystals, *Phys. Rev. B* **76**, 214404 (2007).
- [27] S. Hayami and H. Kusunose, Microscopic description of electric and magnetic toroidal multipoles in hybrid orbitals, *J. Phys. Soc. Jpn.* **87**, 033709 (2018).
- [28] H. Kusunose, Description of multipole in *f*-electron systems, *J. Phys. Soc. Jpn.* **77**, 064710 (2008).
- [29] P. Santini, S. Carretta, G. Amoretti, R. Caciuffo, N. Magnani, and G. H. Lander, Multipolar interactions in *f*-electron systems: The paradigm of actinide dioxides, *Rev. Mod. Phys.* **81**, 807 (2009).
- [30] L. Fu, Parity-Breaking Phases of Spin-Orbit-Coupled Metals with Gyrotropic, Ferroelectric, and Multipolar Orders, *Phys. Rev. Lett.* **115**, 026401 (2015).
- [31] A. Paramekanti, D. D. Maharaj, and B. D. Gaulin, Octupolar order in *d*-orbital Mott insulators, *Phys. Rev. B* **101**, 054439 (2020).
- [32] L. Šmejkal, J. Železný, J. Sinova, and T. Jungwirth, Electric Control of Dirac Quasiparticles by Spin-Orbit Torque in an Antiferromagnet, *Phys. Rev. Lett.* **118**, 106402 (2017).
- [33] P. Liu, J. Li, J. Han, X. Wan, and Q. Liu, Spin-Group Symmetry in Magnetic Materials with Negligible Spin-

- Orbit Coupling, *Phys. Rev. X* **12**, 021016 (2022).
- [34] J. Yang, Z.-X. Liu, and C. Fang, Symmetry invariants in magnetically ordered systems having weak spin-orbit coupling, [arXiv:2105.12738](https://arxiv.org/abs/2105.12738) (2021).
- [35] C.-K. Chiu and A. P. Schnyder, Classification of reflection-symmetry-protected topological semimetals and nodal superconductors, *Phys. Rev. B* **90**, 205136 (2014).
- [36] A. A. Soluyanov, D. Gresch, Z. Wang, Q. Wu, M. Troyer, X. Dai, and B. A. Bernevig, Type-II Weyl semimetals, *Nature (London)* **527**, 495 (2015).
- [37] C. Fang, M. J. Gilbert, X. Dai, and B. A. Bernevig, Multi-Weyl Topological Semimetals Stabilized by Point Group Symmetry, *Phys. Rev. Lett.* **108**, 266802 (2012).
- [38] R. Schmitz, O. Entin-Wohlman, A. Aharony, A. B. Harris, and E. Müller-Hartmann, Magnetic structure of the Jahn-Teller system LaTiO_3 , *Phys. Rev. B* **71**, 144412 (2005).
- [39] E. Bousquet and N. Spaldin, Induced Magnetoelectric Response in $Pnma$ Perovskites, *Phys. Rev. Lett.* **107**, 197603 (2011).
- [40] Z. Wang, D. Gautreau, T. Birol, and R. M. Fernandes, Strain-tunable metamagnetic critical endpoint in Mott insulating rare-earth titanates, *Phys. Rev. B* **105**, 144404 (2022).
- [41] K. Samanta, M. Ležaić, M. Merte, F. Freimuth, S. Blügel, and Y. Mokrousov, Crystal Hall and crystal magnetooptical effect in thin films of SrRuO_3 , *J. Appl. Phys.* **127**, 213904 (2020).
- [42] E. Bousquet and N. Spaldin, Induced Magnetoelectric Response in $Pnma$ Perovskites, *Phys. Rev. Lett.* **107**, 197603 (2011).
- [43] T. Birol, N. A. Benedek, H. Das, A. L. Wysocki, A. T. Mulder, B. M. ABBETT, E. H. Smith, S. Ghosh, and C. J. Fennie, The magnetoelectric effect in transition metal oxides: Insights and the rational design of new materials from first principles, *Curr. Opin. Solid State Mater. Sci.* **16**, 227 (2012).
- [44] L. Vistoli, W. Wang, A. Sander, Q. Zhu, B. Casals, R. Cichelero, A. Barthélémy, S. Fusil, G. Herranz, S. Valencia, R. Abrudan, E. Weschke, K. Nakazawa, H. Kohno, J. Santamaria, W. Wu, V. Garcia, and M. Bibes, Giant topological Hall effect in correlated oxide thin films, *Nat. Phys.* **15**, 67 (2019).
- [45] M. Naka, Y. Motome, and H. Seo, Anomalous Hall effect in antiferromagnetic perovskites, *Phys. Rev. B* **106**, 195149 (2022).
- [46] S. Hayami, Y. Yanagi, and H. Kusunose, Bottom-up design of spin-split and reshaped electronic band structures in antiferromagnets without spin-orbit coupling: Procedure on the basis of augmented multipoles, *Phys. Rev. B* **102**, 144441 (2020).
- [47] D. M. Hatch and H. T. Stokes, *INVARIANTS*: program for obtaining a list of invariant polynomials of the order-parameter components associated with irreducible representations of a space group, *J. Appl. Crystallogr.* **36**, 951 (2003).
- [48] H. T. Stokes, D. M. Hatch, and B. J. Campbell, *INVARIANTS, ISOTROPY Software Suite*, iso.byu.edu, (2022).
- [49] C. Platt, W. Hanke, and R. Thomale, Functional renormalization group for multi-orbital Fermi surface instabilities, *Adv. Phys.* **62**, 453 (2013).
- [50] D.-F. Shao, S.-H. Zhang, G. Gurung, W. Yang, and E. Y. Tsymlal, Nonlinear Anomalous Hall Effect for Néel Vector Detection, *Phys. Rev. Lett.* **124**, 067203 (2020).
- [51] H. Chen, T.-C. Wang, D. Xiao, G.-Y. Guo, Q. Niu, and A. H. MacDonald, Manipulating anomalous Hall antiferromagnets with magnetic fields, *Phys. Rev. B* **101**, 104418 (2020).
- [52] A. Knoll and C. Timm, Classification of Weyl points and nodal lines based on magnetic point groups for spin- $\frac{1}{2}$ quasiparticles, *Phys. Rev. B* **105**, 115109 (2022).
- [53] X. Zhou, W. Feng, R.-W. Zhang, L. Smejkal, J. Sinova, Y. Mokrousov, and Y. Yao, Crystal Thermal Transport in Altermagnetic RuO_2 , [arXiv:2305.01410](https://arxiv.org/abs/2305.01410) (2023).
- [54] A. S. Patri, A. Sakai, S. Lee, A. Paramekanti, S. Nakatsuji, and Y. B. Kim, Unveiling hidden multipolar orders with magnetostriction, *Nat. Commun.* **10**, 4092 (2019).
- [55] V. Stanev, B. S. Alexandrov, P. Nikolić, and Z. Tešanović, Robust accidental nodes and zeros and critical quasiparticle scaling in iron-based multiband superconductors, *Phys. Rev. B* **84**, 014505 (2011).
- [56] R. M. Fernandes and J. Schmalian, Scaling of nascent nodes in extended- s -wave superconductors, *Phys. Rev. B* **84**, 012505 (2011).
- [57] M. Khodas and A. V. Chubukov, Vertical loop nodes in iron-based superconductors, *Phys. Rev. B* **86**, 144519 (2012).
- [58] B. Mazidian, J. Quintanilla, A. D. Hillier, and J. F. Annett, Anomalous thermodynamic power laws near topological transitions in nodal superconductors, *Phys. Rev. B* **88**, 224504 (2013).
- [59] A. V. Chubukov, O. Vafek, and R. M. Fernandes, Displacement and annihilation of Dirac gap nodes in d -wave iron-based superconductors, *Phys. Rev. B* **94**, 174518 (2016).
- [60] I. I. Mazin, Notes on altermagnetism and superconductivity, [arXiv:2203.05000](https://arxiv.org/abs/2203.05000) (2022).
- [61] J. A. Ouassou, A. Brataas, and J. Linder, Josephson effect in altermagnets, [arXiv:2301.03603](https://arxiv.org/abs/2301.03603) (2023).
- [62] S.-B. Zhang, L.-H. Hu, and T. Neupert, Finite-momentum Cooper pairing in proximitized altermagnets, [arXiv:2302.13185](https://arxiv.org/abs/2302.13185) (2023).
- [63] C. Sun, A. Brataas, and J. Linder, Andreev reflection in altermagnets, [arXiv:2303.14236](https://arxiv.org/abs/2303.14236) (2023).
- [64] M. Papaž, Andreev reflection at altermagnet/superconductor interface, [arXiv:2305.03856](https://arxiv.org/abs/2305.03856) (2023).
- [65] D. Zhu, Z.-Y. Zhuang, Z. Wu, and Z. Yan, Topological Superconductivity in Two-Dimensional Altermagnetic Metals, [arXiv:2305.10479](https://arxiv.org/abs/2305.10479) (2023).
- [66] S. A. A. Ghorashi, T. L. Hughes, and J. Cano, Altermagnetic Routes to Majorana Modes in Zero Net Magnetization, [arXiv:2306.09413](https://arxiv.org/abs/2306.09413) (2023).
- [67] G. Kresse and J. Hafner, Ab initio molecular dynamics for liquid metals, *Phys. Rev. B* **47**, 558 (1993).
- [68] G. Kresse and J. Furthmüller, Efficiency of ab-initio total energy calculations for metals and semiconductors using a plane-wave basis set, *Comput. Mater. Sci.* **6**, 15 (1996).
- [69] G. Kresse and J. Furthmüller, Efficient iterative schemes for ab initio total-energy calculations using a plane-wave basis set, *Phys. Rev. B* **54**, 11169 (1996).
- [70] J. P. Perdew, K. Burke, and M. Ernzerhof, Generalized Gradient Approximation Made Simple, *Phys. Rev. Lett.* **77**, 3865 (1996).
- [71] S. V. Gallego, E. S. Tasci, G. de la Flor, J. M. Perez-Mato, and M. I. Aroyo, Magnetic symmetry in the Bilbao Crystallographic Server: a computer program to provide systematic absences of magnetic neutron diffraction, *J.*

[Appl. Crystallogr.](#) **45**, 1236 (2012).
[72] C.-K. Chiu, J. C. Y. Teo, A. P. Schnyder, and S. Ryu,

Classification of topological quantum matter with symmetries, [Rev. Mod. Phys.](#) **88**, 035005 (2016).